Wegener Center for Climate and Global Change
University of Graz
Leechgasse 25, A-8010 Graz, Austria

Atmospheric Remote Sensing and Climate System Research Group
CHAMPCLIM Project Report

WegCenter/UniGraz Technical Report for FFG-ALR No. 1/2006

FFG-ALR Study:

CHAMPCLIM – Radio Occultation Data Analysis Advancement and Climate Change Monitoring Based on the CHAMP/GPS Experiment

[Contract No: ASAP-WV-203/05 – September 2005]

Processing Report
[WP4: MONITOR]

Processing System for Provision of CHAMP Radio Occultation Based Climatologies

M. Borsche, U. Foelsche, A.K. Steiner, A. Gobiet, B.C. Lackner, B. Pirscher, and G. Kirchengast

Wegener Center for Climate and Global Change (WegCenter),
University of Graz, Graz, Austria

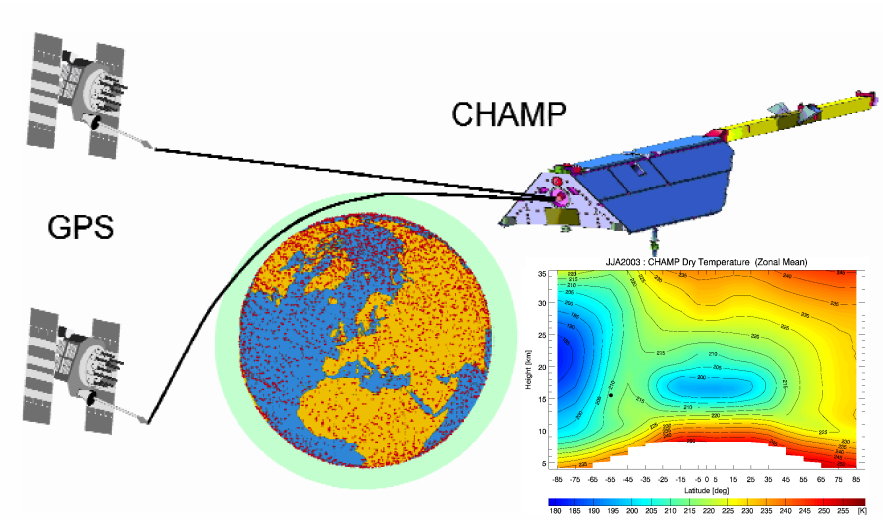

February 2006

Contents

List of Abbreviations

CCRv22	CHAMPCLIM Retrieval version 2.2
CCRv23	CHAMPCLIM Retrieval version 2.3
CHAMP	Challenging Minisatellite Payload
CHAMPCLIM	Radio Occultation Data Analysis Advancement and Climate Change Monitoring based on the CHAMP/GPS Experiment - research project in the Austrian Space Appl. Programme (ASAP) carried out by WegCenter/UniGraz
DJF	winter season (December, January, February)
ECMWF	European Centre for Medium-Range Weather Forecasts
EGM 96	spherical harmonic Earth Gravitational potential Model 1996
ENVISAT	Environmental Satellite (of the European Space Agency ESA)
GFZ	GeoForschungsZentrum (Potsdam)
GNSS	Global Navigation Satellite System
JJA	summer season (June, July, August)
MIPAS	Michelson Interferometer for Passive Atmospheric Sounding
MSIS	Mass Spectrometer and Incoherent Scatter Radar (model)
MSISE-90	Mass-Spectrometer-Incoherent-Scatter model, extended version 1990 (Hedin, 1991)
NIMA	National Imagery and Mapping Agency
NASA	U.S. National Aeronautics and Space Administration
RO	Radio Occultation
UTC	Coordinated Universal Time
VAR	Variational assimilation (usually 1-, 2-, 3- or 4-D)
WegCenter	Wegener Center for Climate and Global Change, University of Graz, Austria
WegCenter/ECMWF	RO retrieval scheme using operational ECMWF analyses as background information
WegCenter/MSIS	RO retrieval scheme using the MSISE-90 climatology as background information
WMO	World Meteorological Organization

1 Introduction

Increasing evidence suggests that the Earth's climate is significantly influenced by human activities (Houghton *et al.*, 2001). While there is little doubt that the Earth's surface temperature has risen by about 0.6° C during the 20th century, the amount and even the existence of temperature trends in the troposphere are still under debate (e.g. Christy and Spencer, 2003; Vinnikov and Grody, 2003). Additional high quality observations of the atmosphere are therefore particularly required in this context. The Global Navigation Satellite System (GNSS) radio occultation (RO) technique has the potential to substantially contribute to this scientific challenge. For a detailed description of the RO technique see, e.g., the reviews of Kursinski *et al.* (1997) and Steiner *et al.* (2001).

With respect to climate studies, one of the most important properties of the RO technique is the expected long-term stability of RO data. It is achieved since precise atomic clocks are the basis for accurate measurements during each single occultation event, independent of whether two events are separated by an hour or by decades. Unlike many traditional satellite data, RO data are essentially self-calibrated as the measurement principle is basically counting of wave cycles (including fractional ones).

The climate monitoring utility of a GNSS occultation observing system has not yet been tested due to the lack of long-term measurements for such a study. The CHAMP (Challenging Minisatellite Payload) RO data provide the very first opportunity to create real RO based climatologies. Continuous data are available since 2001, the mission is expected to last until 2007. Wickert *et al.* (2005b) give an overview of the CHAMP RO experiment, information on the current status can be found in Wickert *et al.* (2005a).

The prime objective of the CHAMPCLIM project is to help ensure that the CHAMP/GPS RO data are exploited in the best possible manner for climate monitoring by addressing three areas: 1) CHAMP RO data and algorithms validation, 2) CHAMP/GPS-based RO data processing advancements in order to optimize the climate utility of the data, and 3) CHAMP/GPS-based monitoring of climate variability and change, respectively. This report is a documentation of the processing system setup and related error estimation work in the context of the climate monitoring work during the second part of the project (CHAMPCLIM-2 project). Here, some efforts are still concentrated on further advancements of the CHAMP retrieval algorithm (calculation of tropopause parameters and height reference to the geoid were added), whereas the main work is focused on setting up and creating the processing system for provision of RO based climatologies and on error characterization of the climatologies.

In Section 2.1 the processing system is introduced and characterized focusing on further advancements of the retrieval algorithm. Section 2.2 explains how the climatological processing is set up and in Section 2.3 we present representative processing products in terms of climatologies showing CHAMP and ECMWF climatologies for the winter season December, January, and February 2002/03 (DJF 0203) and for the summer season June, July, August 2003 (JJA 2003) as well as their corresponding error fields of sampling error, measurement error (bias), standard deviation, and total error. Furthermore, in section 3.1, results of an empirical error analysis of CHAMP profiles of refractivity, pressure, geopotential height, and temperature are discussed, which are important to understand the quality of the derived climatologies. Finally, in section 3.2, estimations of the local time-related error due to the discrete spatio-temporal sampling of the CHAMP satellite are presented, which are important for the climate data quality as well.

2 Processing System Description and Climatology Products

The CHAMPCLIM retrieval chain starts with CHAMP data provision by GFZ Potsdam. After the GFZ-internal calibration process (Schmidt *et al.*, 2005) on the original data, ∼180 atmospheric excess phase profiles remain per day and are transferred to WegCenter. As reference data, 6-hourly analysis fields of the European Centre for Medium-Range Weather Forecasts (ECMWF) are used (four time layers per day; 6 UTC, 12 UTC, 18 UTC, 24 UTC), which are downloaded directly from ECMWF.

The RO retrieval scheme applied to these data is developed at WegCenter (Steiner *et al.*, 2004; Gobiet and Kirchengast, 2004b) in close connection with developments of the End-to-end GNSS Occultation Performance Simulator (EGOPS) (Kirchengast *et al.*, 2002). The retrieval is especially focused on minimizing the bias of atmospheric parameters. Table 1 provides an overview on the main aspects of the retrieval scheme. The retrieval implements statistical optimization in two different ways, one of which uses the MSISE-90 climatology (Hedin, 1991) (WegCenter/MSIS) and the other operational ECMWF analysis fields (WegCenter/ECMWF) as background information. This background information is integrated into the retrieval only at one point (bending angle level), resulting in well defined error characteristics. Another main aspect of the retrieval is that the hydrostatic integral is initialized only once from a pressure guess at a height of 120 km (Gobiet and Kirchengast, 2004b).

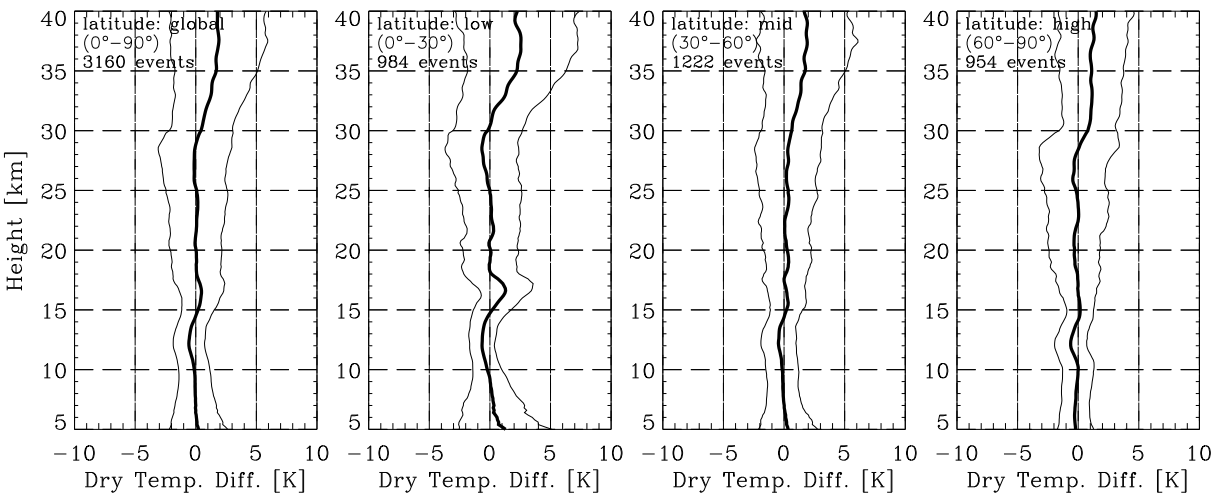

Figure 1: WegCenter/ECMWF retrieval of a selected validation set of profiles compared to ECMWF analysis fields. Bias (bold) and bias ± standard deviation profiles (light) of dry temperature. Panels divide events into global, low-, mid-, and high-latitude regions. Above 30 km a significant deviation of ECMWF from CHAMP data is observed.

As has already been reported in Gobiet *et al.* (2004) the retrieval scheme was validated against independent data. For these validation purposes, a subset of the retrieved CHAMP data was compared at refractivity and dry temperature level to various data sources including data from the Michelson Interferometer for Passive Atmospheric Sounding (MIPAS) on the Environment Satellite (ENVISAT). This analysis was carried out considering 3160 CHAMP occultation events and 184 co-located ENVISAT/MIPAS events, observed in a 20-day period during September 2002. Here, the WegCenter/ECMWF retrieval (Figure 1) and the validation of the WegCenter/ECMWF retrieval compared to ENVISAT/MIPAS data (Figure 2) are shown. The Figures depict the bias (bold) and the bias ± standard deviation profiles (light) of dry temperature.

As can be read in more detail in Gobiet *et al.* (2004), the main finding of the validation of the WegCenter/ECMWF against independent data was that the WegCenter/ECMWF retrieval

Table 1: Overview of the WegCenter CHAMP-RO retrieval schemes (EGOPS/CCR Versions 2.2 and 2.3)

	WegCenter/MSIS	WegCenter/ECMWF
Outlier Rejection and Smoothing	"$3\,\sigma$" outlier rejection on phase delays and smoothing using regularization (third order norm, regularization parameter $=10^{(\text{sampling rate}/10)}$) (Syndergaard, 1999)	Like WegCenter/MSIS
Bending Angle Retrieval	Geometric Optics retrieval	Like WegCenter/MSIS
Ionospheric Correction	Linear combination of bending angles (Vorob'ev and Krasnil'nikova, 1994). Correction is applied to low-pass filtered bending angles ($\sim$1 km sliding average), L1 high-pass contribution is added after correction (Hocke *et al.*, 2003). L2 bending angles <15 km derived via L1-L2 extrapolation.	Like WegCenter/MSIS
Bending Angle Initialization	Statistical optimization of bending angles from 30 km to 120 km. Vertical correlated background (corr. length $L = 6$ km) and observation ($L = 1$ km) errors. Observational error estimated from observed profile >65 km. Background error: 15 %. Background information: MSISE-90 (Hedin, 1991) best-fit profile, bias corrected (Gobiet and Kirchengast, 2004b).	Like WegCenter/MSIS, but co-located bending angle profile derived from ECMWF operational analysis as background information (above ~ 60 km: MSISE-90). No further pre-processing.
Hydrostat. Integral Init.	At 120 km: pressure $= p$(MSISE-90)	Like WegCenter/MSIS
Humidity Retrieval	Like WegCenter/ECMWF	Optional: 1D-Var using ECMWF short-range forecasts as background
Quality Control	Like WegCenter/ECMWF	Refractivity 5 km$-$35 km: $\Delta N/N < 10\,\%$; Temperature 8 km$-$25 km: $\Delta T < 20$ K. Reference: ECMWF operational analysis (T42L60)

compared to MIPAS temperatures above 30 km is not warm biased (see Figure 2) as are the CHAMP dry temperatures compared to ECMWF (see Figure 1). This leads to the conclusion that there is still significant information content in the CHAMP data exceeding 30 km. However, in that height neither of the data is particularly good (confer Section 3.2).

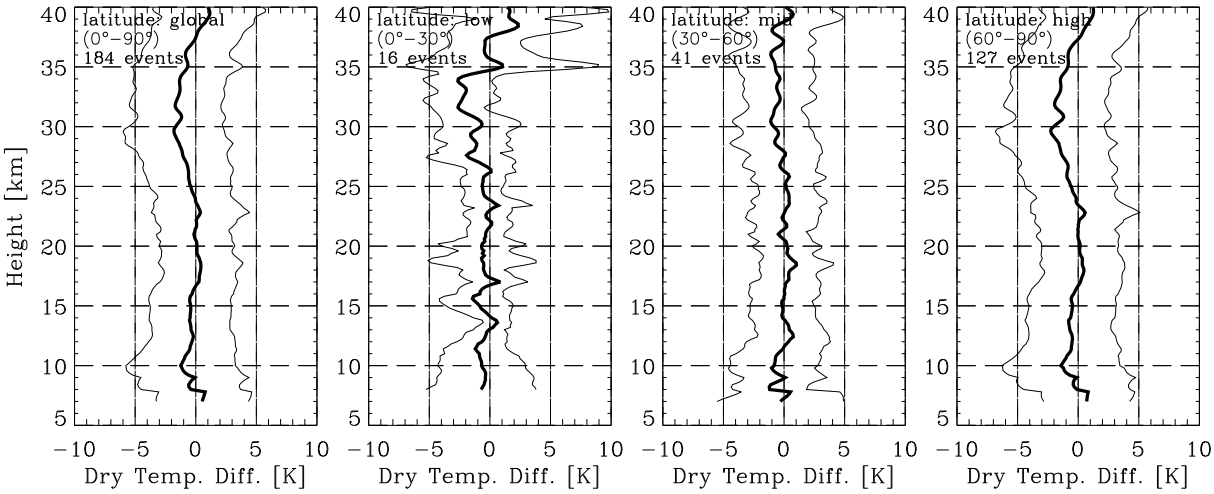

Figure 2: WegCenter/ECMWF retrieval of a selected validation set of profiles relative to coinciding temperature profiles from ENVISAT/MIPAS. Bias (bold) and bias ± standard deviation profiles (light) of dry temperature. Panels divide events into global, low-, mid-, and high-latitude regions. Above 30 km no signficant deviations between the two correlative datasets are observed.

2.1 Characterization of the Processing System

2.1.1 Status of the Pre-Operational Processing System

Recent work at WegCenter/UniGraz has concentrated on the establishment of a pre-operational processing system, which includes data transfer from GFZ and ECMWF, retrieval of atmospheric parameters, quality control, creation of climatologies, and storage of the data. At this stage, the processing system operates in an automated way up to the RO retrieval and quality control, whilst the automated creation of the climatologies will be integrated in the very near future. The aim is to establish a data stream from GFZ which downloads 7-day packages of data within a time delay of two days and to provide the final CHAMPCLIM climatology products within a timeliness limit of 14 days.

Up to the present, CHAMP data have been transferred manually via a secure ftp connection from GFZ to WegCenter/UniGraz. So far, the data transferred cover a time span from September 2001 to September 2005. The first six months of this data set span a period of sparse global sampling amounting to only about 50 to 100 events per day. Nevertheless, this sampling is sufficient for creating zonal mean seasonal climatologies.

ECMWF analysis fields have been downloaded directly from ECMWF comprising 6-hourly fields with four time layers at 6 UTC, 12 UTC, 18 UTC, 24 UTC including the parameters geopotential, temperature, specific humidity, and logarithm of surface pressure. ECMWF data covering the same time span as the CHAMP data have been transferred and stored locally at WegCenter/UniGraz. The processing of the data is finished for the time period March 2002 to May 2005 covering thirteen seasons or more than three years. The retrieval of the data is an ongoing process and is being performed on the newly received data from September 2001 to February 2002 as well as on the data starting from June 2005.

2.1.2 Enhancement of the Profile Retrieval: Tropopause Parameters

The current version of the retrieval, CHAMPCLIM Retrieval version 2.3 (CCRv23), has implemented mainly three new features compared to the last version as described in Gobiet *et al.* (2004): First, calculation of tropopause parameters such as lapse rate tropopause height and temperature and cold point tropopause height and temperature, secondly, the calculation of the geoid height of the profiles, and finally surface parameters as well as satellite specific parameters were written out. The tropopause parameters serve new studies whereas the switch to reference the profiles to the geoid as opposed to reference the profiles to the reference ellipsoid improves the results systematically. The newly written out surface parameters comprise the surface orography altitude at the position of the event, the surface (2 m) temperature, the skin temperature, and the surface pressure and humidity. Satellite parameters include the azimuth as well as the inclination of the occultation plane. Both the surface and the satellite parameters will also be used in future studies.

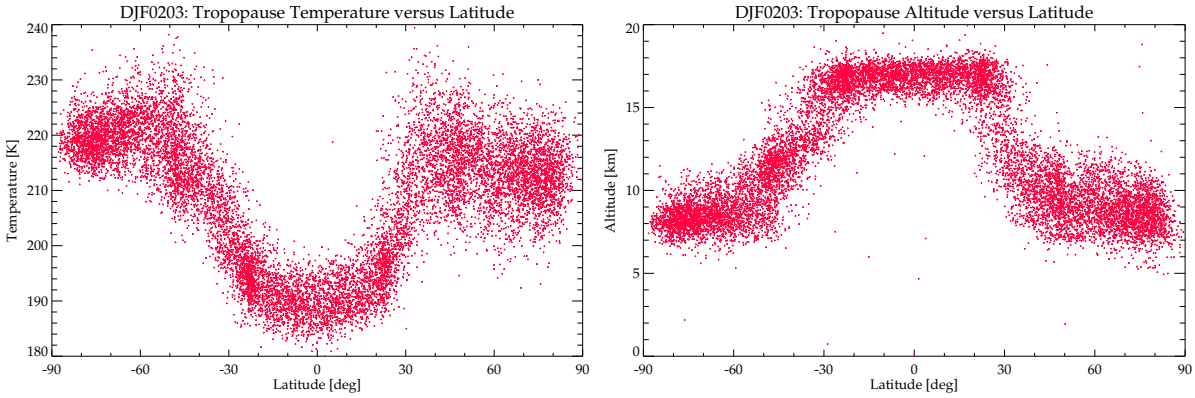

Figure 3: Lapse rate tropopause temperature (left) and height (right) are shown for season DJF 0203 versus latitude. The low-latitude tropopause ($\pm 30°$) is even colder than the northern winter polar tropopause and exhibits heights of 16 km to 18 km. Additionally it is the region with the least spreading in height.

The lapse rate tropopause was calculated according to the definition of the World Meteorological Organization (WMO). Here, the tropopause is defined as the lowest level at which the temperature lapse rate is less than $2\,\mathrm{K\,km^{-1}}$ and the lapse rate average between this level and the next two kilometers does not exceed $2\,\mathrm{K\,km^{-1}}$ (WMO, 1957). Preliminary results are shown in Figures 3 and 4 in which for the winter season December, January, and February 2002/03 (DJF 0203) and for the summer season June, July, August 2003 (JJA 2003) the distribution for the tropopause temperature (left) and height (right) for all CHAMP profiles are depicted in a latitude-temperature and latitude-height plot, respectively. In the low-latitude region ($\pm 30°$) the lapse rate tropopause is clearly defined with the criterion from WMO which can be inferred from the narrow spreading of tropopause height. However, in mid-latitudes and especially in the high-latitude winter regions this criterion seems to be more difficult to meet due to the special winter atmospheric layering. Here the tropopause parameters vary a lot for each profile. The same is true for the cold point tropopause temperature and height which is defined as the coldest point of the profile in the upper troposphere and lower stratosphere region (not shown here).

2.1.3 Enhancement of the Profile Retrieval: Geoid Altitudes

The second new feature implemented in CCRv23 is the calculation of the height above the geoid for determining the vertical grid of the profiles.

The ECMWF analysis fields are referenced to the geoid whereas the CHAMP profiles were up to now referenced to the reference ellipsoid. However, the geoid can differ compared to the

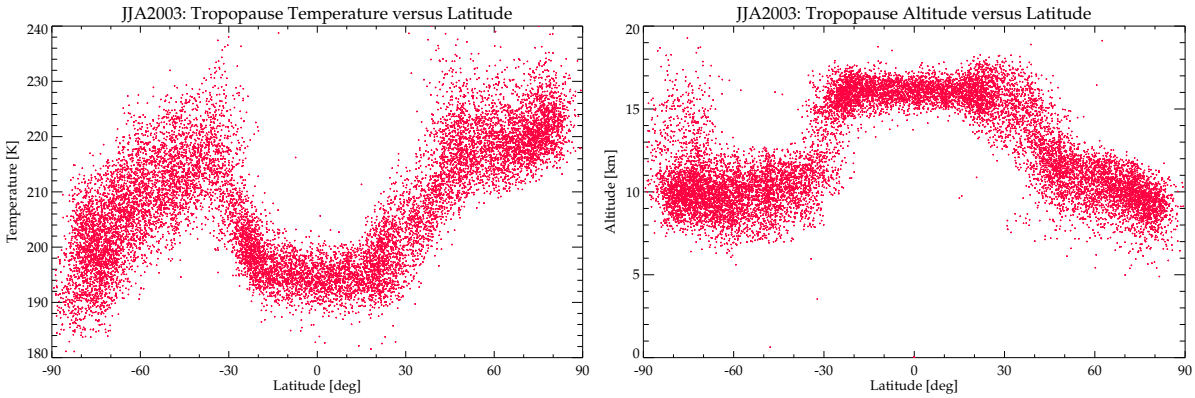

Figure 4: Lapse rate tropopause temperature (left) and height (right) are shown for season JJA 2003 versus latitude. In this season the southern winter polar tropopause is colder than the tropical tropopause. Also, the spreading of tropopause heights increases significantly in the winter polar region whereas in the low-latitude region the spreading is rather small. (The lower-bound "steps" in tropopause height at some latitudes are artefacts due to the initialization height setting of this version of the tropopause algorithm; this will be rectified in future versions.)

reference ellipsoid up to about 85 m above (around the island of New Guinea) and up to about 105 m below (northern Indian Ocean) as can be seen in Figure 5 which depicts the difference between the geoid compared to the reference ellipsoid in meter. As long as the CHAMP profiles were referenced to the reference ellipsoid a systematic bias was introduced. Because in the worst case the profiles could be shifted more than 100 m to each other the bias could in theory amount up to 0.65 K due to the vertical adiabatic temperature gradient in the troposphere of 0.65 K per 100 m (temperature gradients in the lower stratosphere are much smaller).

To demonstrate this theory in practice exemplarily, in Figures 6 and 7 the differences in temperature between CHAMP profiles referenced to the geoid compared to profiles referenced to the reference ellipsoid are shown. Figure 6 depicts the zonal mean of the season JJA 2003 in which the effects on temperature of elevated and depressed landmasses of the geoid cancel each other out. However, instead of using the zonal mean, profiles on a smaller scale using latitude slices show the effect clearly. On the left of Figure 7 a latitude slice centered around 80° E longitude is depicted (including the northern Indian Ocean with deepest depression) and on the right a slice centered around 140° E longitude (including New Guinea with highest elevation). In the first case (depression) the difference is positive in the troposphere because the profiles start lower, and vice versa in the second case (elevation). Obviously, the effect switches in the lower stratosphere, but as mentioned above the vertical temperature gradient is much weaker and therefore the difference is much smaller.

2.2 Setup of RO Based Climatologies

The implementation of the climatologies as final product is pursued in two different ways. On the one hand, a global 3D-Var analysis by assimilation of CHAMP data into ECMWF short-term forecast fields was developed, which is described by Löscher *et al.* (2005). On the other hand, a direct-binning grid strategy is implemented in two modes leading to the final products, which will be the focus of this section.

2.2.1 Vertical Resolution of the Climatologies

For the creation of gridded pure RO based climatologies several factors and requirements concerning the spatial and temporal resolution have to be taken into account. The resolution of a

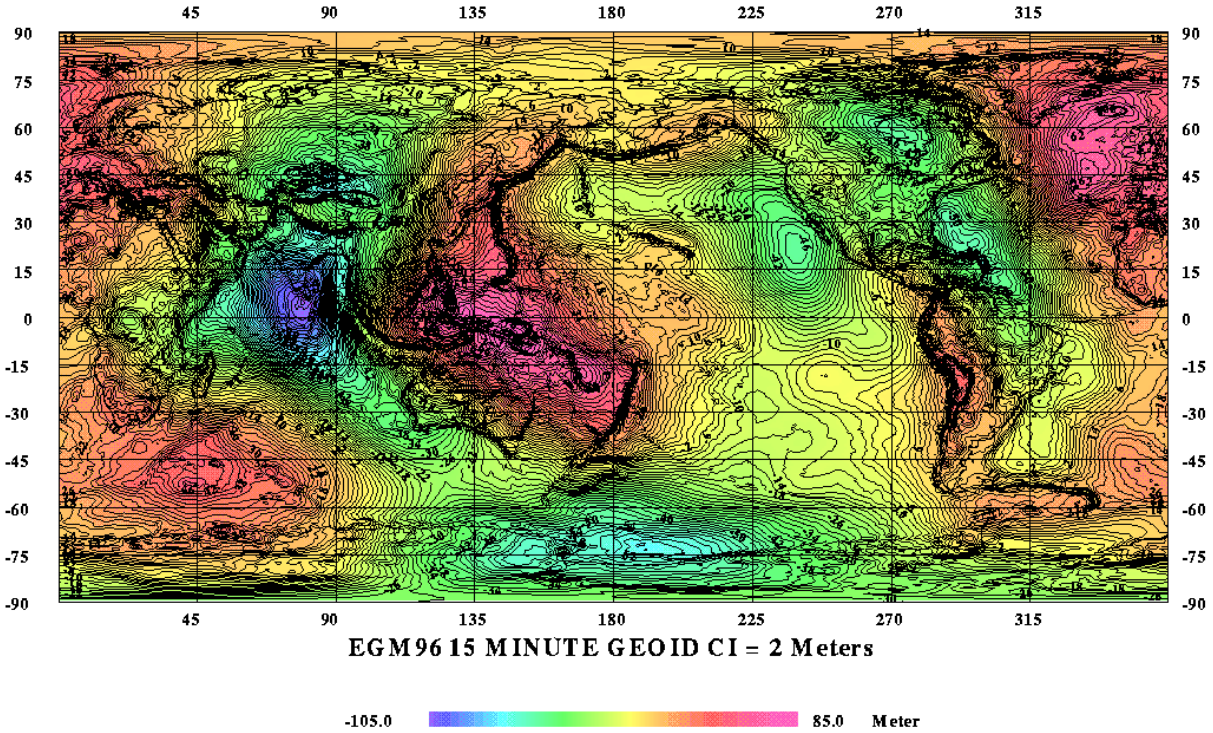

Figure 5: Latitude - Longitude map of the spherical harmonic Earth Gravitational potential Model (EGM 96) by the U. S. National Space and Aeronautics Administration (NASA) and the National Imagery and Mapping Agency (NIMA) with a horizontal resolution of 15×15 arc-Min. The geoid altitude is depicted in meters and ranges from ~ -105 m to $\sim +85$ m.

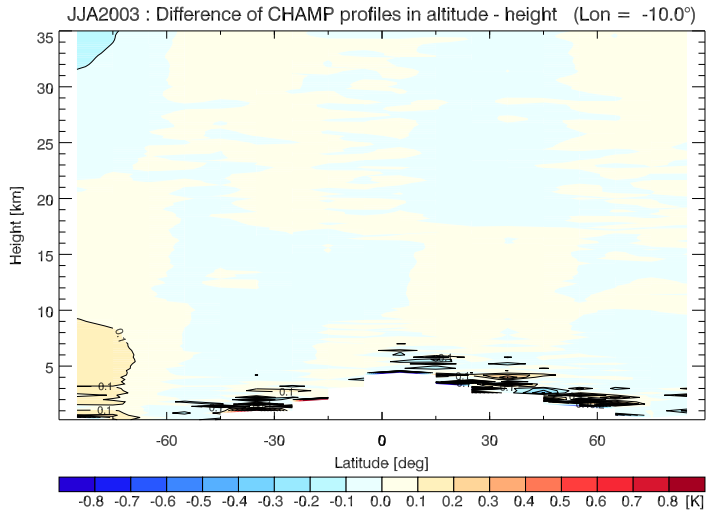

Figure 6: Zonal difference of CHAMP temperature profiles referenced to the geoid compared to temperature profiles referenced to the ellipsoid in the height range from the ground to 35 km. In the zonal mean there is virtually no difference to be observed except for the lower troposphere. The blank space in the low-latitude lower troposphere is due to the lack of CHAMP data in that region.

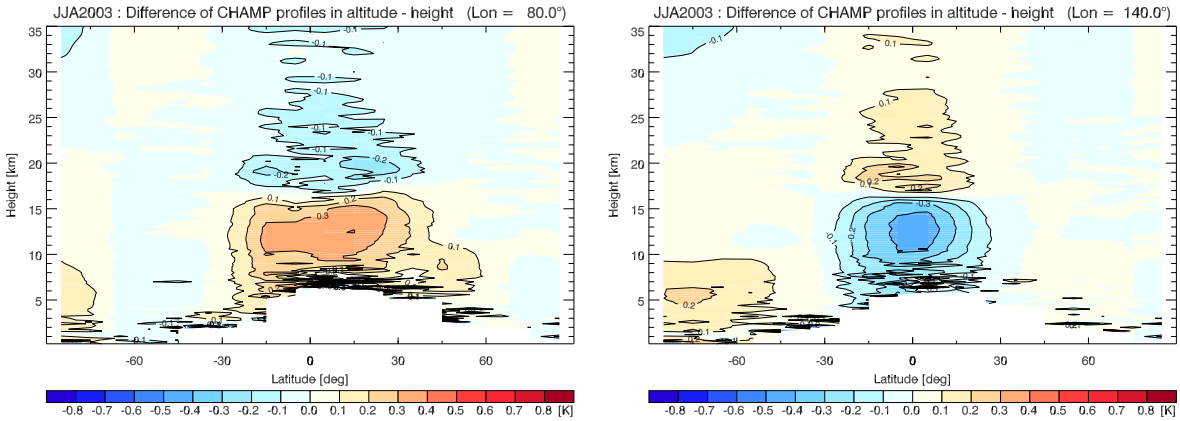

Figure 7: Difference of CHAMP temperature profiles referenced to the geoid compared to profiles referenced to the ellipsoid in the height range from the ground to 35 km for two latitude slices: On the left the latitude slice is centered around 80° E, on the right around 140° E, corresponding to the locations of the greatest depression and highest elevation of the geoid, respectively.

single measurement and the measurement density set the limits for the resolution of any gridded data set derived from measurements. For RO measurements, the vertical resolution amounts to around 1 km to 1.5 km whereas the horizontal resolution in the direction of the ray amounts to about 250 km to 300 km. Since the CHAMP satellite over-samples (higher measurement density than physical resolution) in the order of a factor of ten because of its measurements frequency of 50 Hz, it is possible to provide gridded CHAMP data on a denser vertical grid than it would correspond to the measurement's physical resolution. However, in such a case it must be clearly stated that neighboring values of the grid are not independent from each other.

The physical resolution of the WegCenter/ECMWF retrieval scheme has been determined exemplarily on a test set of 12 CHAMP profiles, for each season one profile from high-, mid-, and low-latitudes, respectively. To determine the vertical resolution of the retrieval scheme the method of the perturbation theory was used. The perturbation theory states that an initial infinitesimal narrow (delta) perturbation of the input to a continuous system will result in a gaussian-like shaped response. The full width at half maximum of the gaussian distribution can then be considered as the inherent resolution of the system. In that manner, each profile was perturbed at phase delay level to determine the resolution of the WegCenter/ECMWF retrieval.

Figure 8 depicts a preliminary result of the perturbation of a CHAMP low latitude profile taken in spring 2003. The first plot (upper left) depicts the delta perturbation at phase delay level. At a time delay which will correspond to a certain height in the temperature plot, the phase delay profile was perturbed with an amplitude of 110 % of the input value. This perturbation propagates through the retrieval system and the response function changes according to the operator used: bending angle retrieval, refractivity retrieval, and finally the temperature retrieval. Because of the Doppler Shift differentiation in the bending angle retrieval the response to the initial perturbation is slant symmetrical - as opposed to a gaussian shaped response of linear operators. After the refractivity and temperature retrievals this shape has changed to a asymmetrical slant response of third order which is far from easy to interpret regarding the intrinsic retrieval resolution.

As is displayed in Figure 8 in the lower right plot at the temperature level, we have narrowed down the meaningful range of the resolution value: The peak-to-peak value represents arguably the highest resolution, whereas the "10 % peak-to-peak" value, which is met where the value of each peak has decreased again to 10 % of its maximum, might be already underestimating the resolution. The difference of these values seems to be a feasible value resulting in 1.33 km for

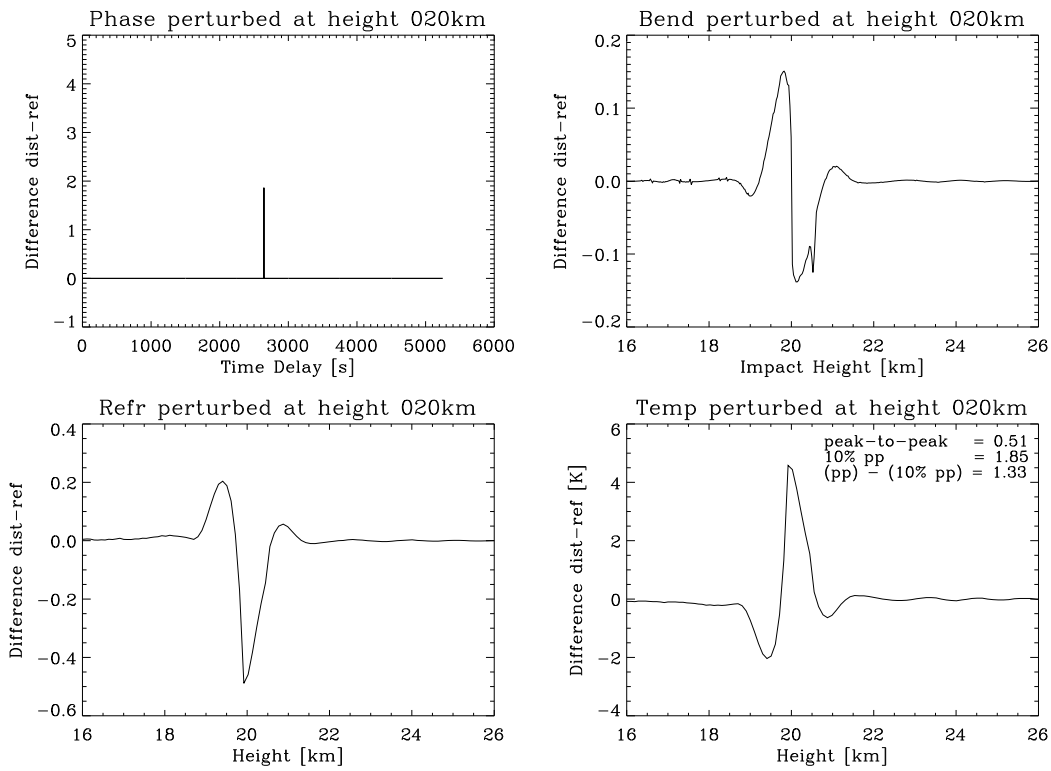

Figure 8: Perturbation of one CHAMP profile at 20 km height. The perturbation was applied at phase delay level in form of a delta perturbation with an amplitude of ∼100 % of the input value. The perturbation propagates through the whole retrieval algorithm until it has become an asymmetrical slant response of third order at temperature level. Displayed are the values of height differences which correspond to the response amplitude at 10 % of peak-to-peak, at peak-to-peak, and at the difference of both. These figures suggest estimates of the vertical resolution of profiles at that height.

the profile displayed at a height of 20 km.

2.2.2 Binning Strategy for the Climatologies

The second consideration for the resolution of a gridded data set is defined by the measurement density and distribution. Each grid cell has to contain sufficient data to ensure the representativeness of the data for the mean location and time of the cell. In the horizontal, the spatial measurement density depends on the temporal averaging period and on geometrical properties of the measurement system. The CHAMP satellite yields some 150 globally distributed atmospheric profiles per day with higher density (referred to equal areas) at high latitudes compared to lower latitudes.

Additionally, it is of interest to evenly sample the diurnal cycle. According to the orbit parameters of CHAMP the diurnal cycle is ideally scanned within ~ 130 days which implies that even seasonal means (90-92 day period) do not ideally sample it. However, error studies focusing on the diurnal effect show that seasonal and even monthly sampling periods are not very much degraded by this sampling error (cf. Section 3.2).

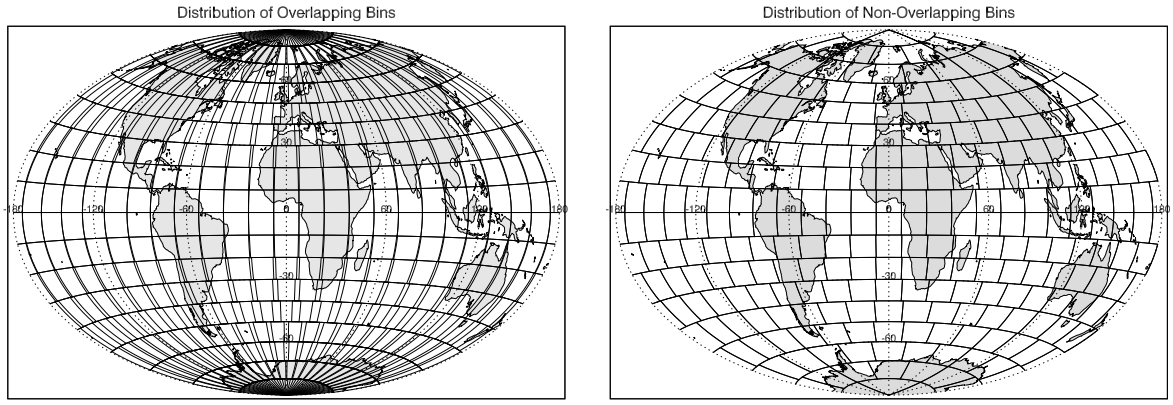

Figure 9: Two modes of binning. Overlapping equal-area bins at a regular 18 lat × 24 lon grid on the left, and non-overlapping almost equal-area bins at 18 lat × lat-dependent lon grid on the right.

The arguments above implied a preliminary setup of global climatologies with a vertical layer each 500 m and a horizontal binning as shown in Figure 9. Shown are two different modes of how to possibly set up climatologies with differing arrangements of equal area bins. Along latitude, both modes have the meridian divided into 18 bins of 10° width. Along longitude, the first mode (left side of Figure 9) uses 24 fixed bins (baseline) at all latitudes leading to bin overlapping, whilst the second mode (right side) uses a latitude-dependent number of bins to obtain non-overlapping almost equal area bins (within $\pm 0.5°$ exact; except for polar latitudes where the latitude extension differs up to 7.9° per bin). While climatologies on the regular grid (lat×lon) are most convenient to handle, comparison to the second mode allows study of the potential relevance of error correlations between overlapping bins.

The prime testbed season was arbitrarily chosen to be JJA 2003. Due to the high inclination of the CHAMP satellite (87.3°) the global event distribution varies from sparse sampling in the equatorial region to high sampling in polar regions. As shown in Figure 10 on the left side illustrating event distribution for a 10°×15° binning for the testbed season, there are sufficient events in the equatorial region for deriving robust statistics as is required for climatologies. As shown in Section 2.3 in Figures 11 and 14 the gridding with 10°×15° bins worked fine on the prime testbed season.

During other seasons, however, there are rare occasions in which an equatorial bin of a

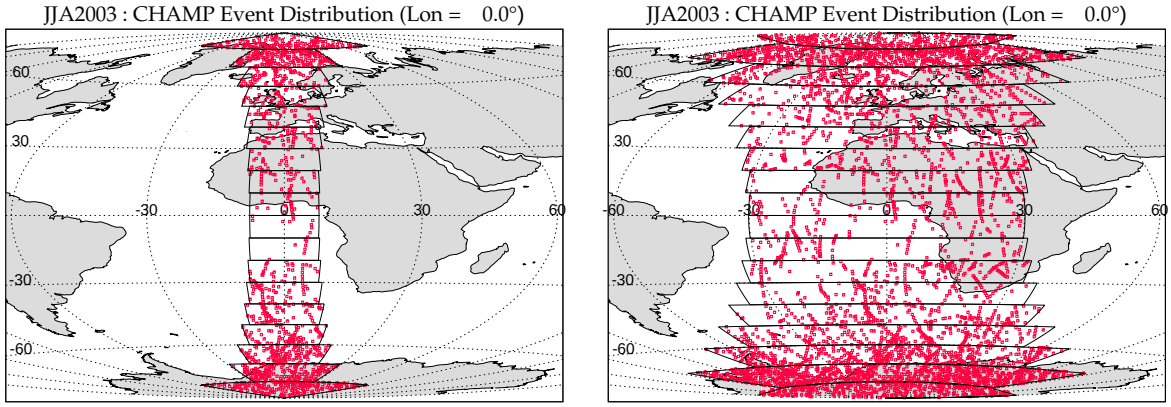

Figure 10: Event distribution in a latitude slice for 10°×15° binning on the left and for 10°×60° binning on the right. Both latitude slices are taken from the summer season JJA 2003 around the prime meridian. In both slices the event distribution has a minimum number around the equator and increases towards the poles.

10°×15° latitude slice does not contain any RO events at all. In monthly latitude slices there are more latitude slices with no events in some bins. Therefore, we have decided to broaden the gridding of the climatologies to 10°×60° binning (18 lat × 6 lon grid). The right side of Figure 10 shows the event distribution of that grid exemplary on the latitude slice of the prime meridian in the testbed season.

2.3 RO Based Climatologies

2.3.1 Gridded Climatologies

A lot of effort has been put into the creation of climatologies and determining their error fields. In this section we exemplarily present two gridded climatologies, one is the prime testbed summer season JJA 2003 and the other the winter season 2002/03 (DJF 0203) as well as their corresponding error fields. To determine the error fields of the CHAMP data, near realistic atmospheric fields as reference data are used. ECMWF operational analyses represent today's best knowledge of the state of the atmosphere and are ideally suited for serving as such reference data sets. In the following, the four daily time layers of ECMWF analysis fields are taken as the true state of the atmosphere, which is assured in most parts of the analysis by the integration of a massive amount of observations into the analysis (ECMWF, 2004), to which CHAMP data are compared to.

With such a reference data set it is possible to separate the total error of the CHAMP climatologies into a sampling error and measurement error (bias). The sampling error is calculated as the difference between the climatological fields obtained from perfect (error-free) profiles at the locations of the RO events and climatological fields derived from the "true" 3D reference fields. The measurement error is calculated via difference error statistics by comparing each CHAMP profile with a co-located reference profile extracted from the ECMWF fields.

In Figures 11, 12, and 13 the CHAMP and ECMWF climatologies for dry temperature in Kelvin are shown together with the corresponding sampling error. They contain the seasons DJF 0203 and JJA 2003 with gridding of 10°×15°, 10°×60°, and zonal means, respectively. To obtain the CHAMP climatological fields, all events of each bin were averaged. ECMWF climatologies are derived from the gridded ECMWF analysis fields. The climatologies are shown in a latitude versus height coordinate system which ranges from the ground to 35 km in height and over the whole meridian in latitude.

At first sight both climatologies are fairly alike to each other and the representation of the

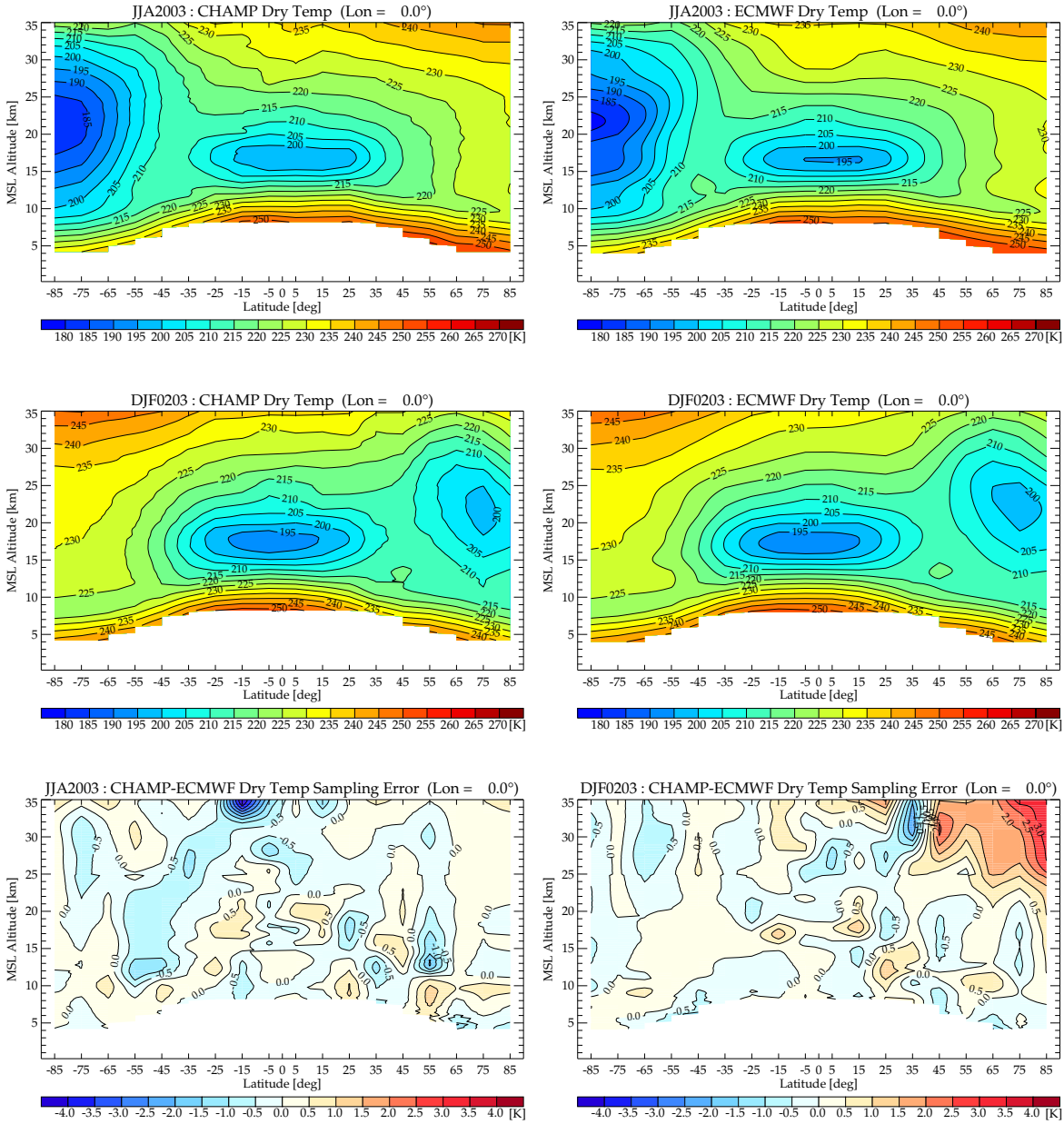

Figure 11: CHAMP and ECMWF climatologies of dry temperature with gridding of $10^\circ \times 15^\circ$ for the JJA 2003 (top row) and DJF 0203 (middle) seasons. The last row shows the corresponding sampling error of the JJA 2003 and DJF 0203 seasons on the left and on the right, respectively.

temperature gradient is as expected. In the troposphere the temperature decreases with increasing height up to the tropopause. The cold tropical tropopause region can be extinguished clearly in both seasons with temperatures as low as $\sim$ 190 K. Above in the low to mid stratosphere, the temperature rises again due to warming by ozone dissociation. In JJA 2003 the austral winter polar vortex has developed with the lowest temperatures in the mid atmosphere reaching as far low as $\sim$180 K. The boreal winter polar vortex does not cool down as much and for DJF 0203 was even warmer than the tropical tropopause region with temperatures just under 200 K.

2.3.2 Sampling Error of Climatologies

The error due to spatial and temporal undersampling of the true evolution of atmospheric fields has been identified as a potential major error source for single-satellite climatologies with the aid of simulation studies (Foelsche *et al.*, 2003). Even with perfect observations at the occultation locations the "measured" climatologies would differ from the "true" ones as the sampling through occultation events is discrete and not dense enough to capture the entire spatio-temporal variability of the atmosphere. Under the assumption that the ECMWF analysis fields (4 time layers per day) represent the true state of the atmosphere, the sampling error is estimated by comparing climatologies derived from the "true" ECMWF profiles at the RO locations with climatologies derived from the "true" 3D ECMWF fields. The sampling errors for each season is shown in the last row of Figures 11, 12, and 13, respectively.

Below 4 km in polar regions and below 8 km in low-latitudes ($\pm 30°$ latitude) the climatologies have been cut-off deliberately. Starting at the poles up to 65° latitude the climatologies reach down to 4 km, the cut-off height increases in 1 km by 10° steps to 8 km height in the low-latitudes (30° north and south). In addition to the height criterion the amount of the profiles in each bin has to be above ten otherwise the bin will be treated as having no data. This cut-off strategy was perused because there is a large "warm" sampling error for dry temperatures. This feature, which has been recognized by Foelsche *et al.* (2006), can be interpreted as a selective "dry sampling error". The tracking of CHAMP signals and the geometric optics retrieval tends to stop at higher altitudes in moist compared to dry conditions. The lowest part of the RO profiles is therefore biased towards dry conditions, resulting in a systematic underrepresentation of the true mean refractivity. When the refractivities are converted to dry temperatures, this systematic error maps into warm-biased mean dry temperatures. This effect is most pronounced at low latitudes, where the event density is particularly low (see Figure 10) due to the high inclination of the CHAMP satellite.

The sampling error decreases with decreasing amount of bins per latitude band as can be seen in the three figures. There is a sufficient amount of events in the $10° \times 15°$ gridding (Figure 11) and the CHAMP climatology can be calculated with acceptable error characteristics. In the JJA 2003 season the sampling error amounts up to ± 1.5 K. For the DJF 0203 season the sampling error is less in general amounting to just above ± 1.0 K except for a region of the boreal winter polar vortex in heights above 20 km in which the sampling error amounts to more than 3.0 K. For the $10° \times 60°$ gridding (Figure 12) the sampling error reduces and only in rare occasions reaches above ± 1.0 K; the huge error in the boreal winter polar vortex has also reduced but still amounts to more than 2.0 K. Finally, in the zonally gridded climatologies (Figure 13) except for patches the sampling error is diminished to below ± 0.5 K; again the boreal winter polar vortex region is an exception with errors ranging from 1 K to 2 K. It is assumed that the high sampling error in high latitudes, which occurs in some other seasons as well, may be related to an uneven sampling within bins located especially in regions with high temperature gradients (around 70° to 80°). By averaging the unevenly distributed events in such a bin a bias is introduced. The investigation of this feature is queued with high priority for immediate study.

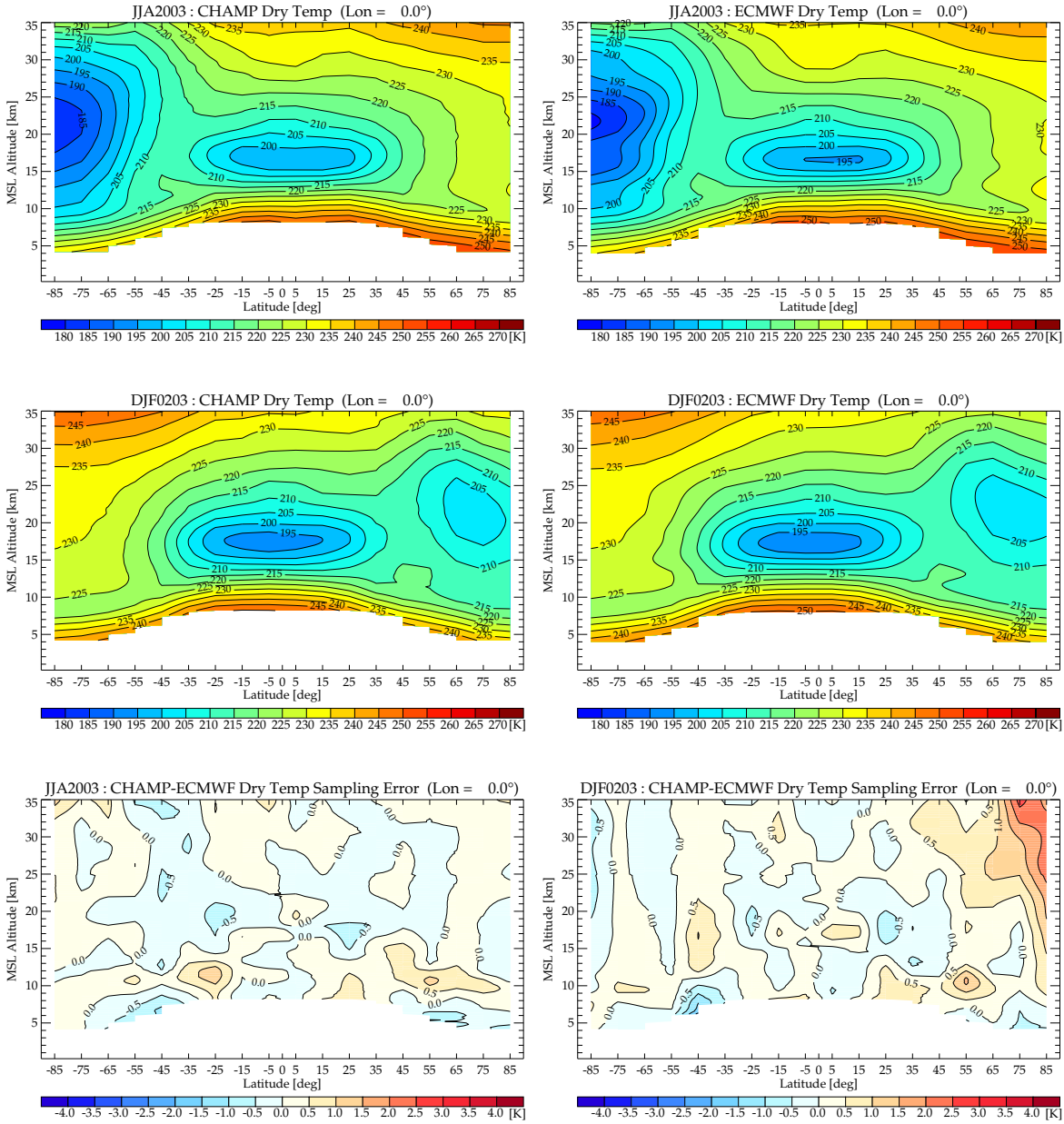

Figure 12: CHAMP and ECMWF climatologies of dry temperature with gridding of $10^\circ \times 60^\circ$ for the JJA 2003 (top row) and DJF 0203 (middle) seasons. The last row shows the corresponding sampling error of the JJA 2003 and DJF 0203 seasons on the left and on the right, respectively.

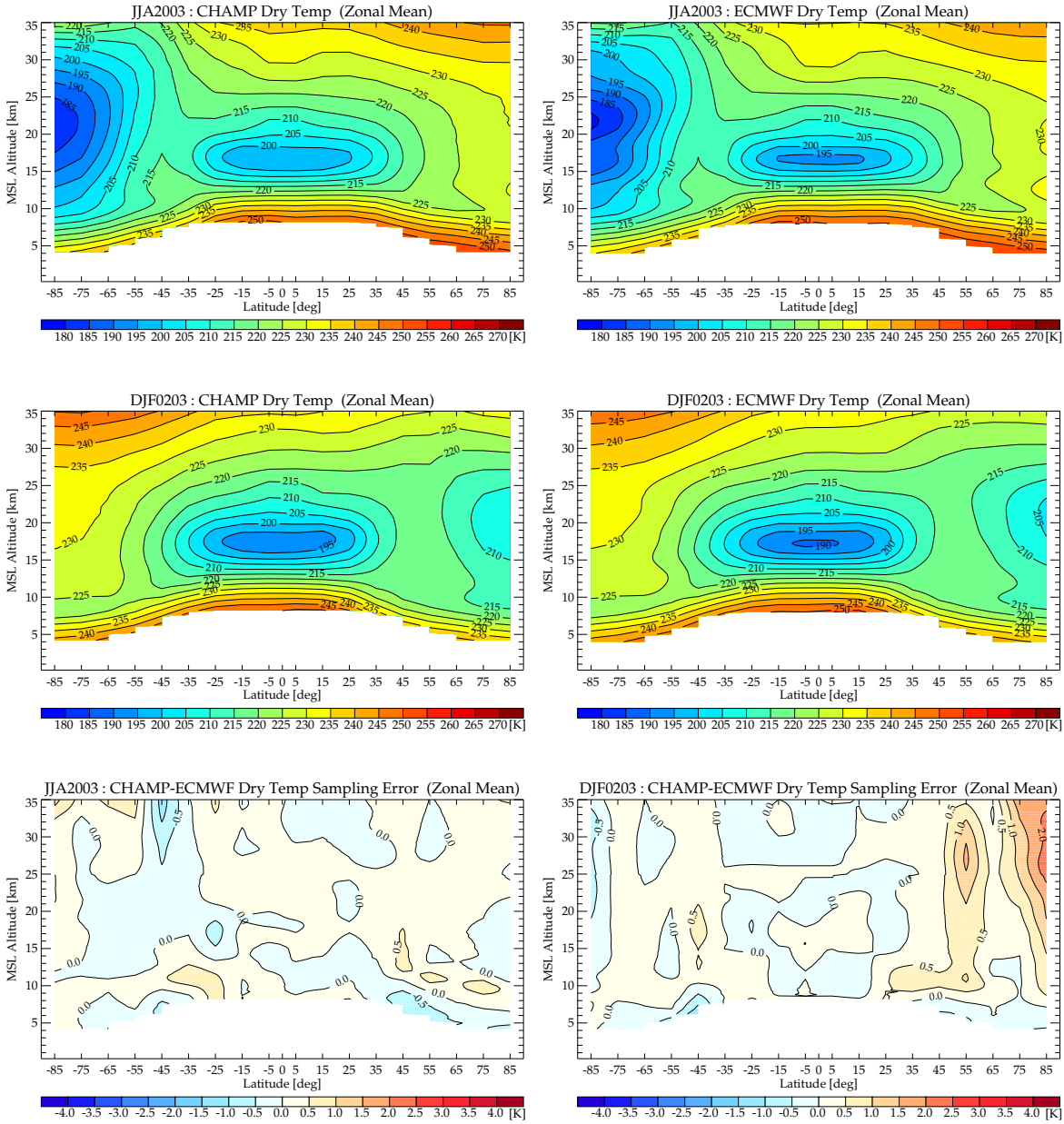

Figure 13: Zonal mean CHAMP and ECMWF climatologies of dry temperature for the JJA 2003 (top row) and DJF 0203 (middle) seasons. The last row shows the corresponding sampling error of the JJA 2003 and DJF 0203 seasons on the left and on the right, respectively.

2.3.3 Measurement and Climatological Error of Climatologies

In Figures 14, 15, and 16 three additional "error" fields for both seasons are shown. In the top row the bias (the mean deviation between CHAMP and ECMWF), in the middle row the standard deviation (square-root of the variance of individual CHAMP-ECMWF difference profiles about the bias profile), and in the bottom row the climatological error (sampling error plus bias) is depicted, respectively. Again, all three figures illustrate the gridding of $10° \times 15°$, $10° \times 60°$, and zonal averaging, respectively. The errors are calculated based on difference profiles, obtained by subtracting from each CHAMP profile the co-located ECMWF profile. The climatological error can be directly determined by computing differences of RO based and "true" reference climatologies.

Being closely related to the sampling error, the climatological error decreases with the decrease in the number of latitude bins in the gridding scheme. On the left side in the last row of Figure 16 the climatological error for the zonal mean of the summer season JJA 2003 is depicted. While differences in the lower troposphere (which have been cut-off) can clearly be attributed to RO errors, the differences above 30 km of about 1 Kelvin and more are most probably due to errors in both CHAMP and ECMWF. At that height the ECMWF analyses are only partly constrained by data and the RO measurement errors start to increase. In the height range in which RO data have the highest quality ($\sim$8 km to $\sim$30 km), the CHAMP and ECMWF climatologies agree, in general, very well with an absolute bias of less than 0.5 K, occasionally peaking at 1 K.

However, two features are eminent: The tropical tropopause region in the CHAMP-derived fields is consistently warmer than the ECMWF analyses. Note that this is only a measurement bias in which no distinct sampling error is involved (compare Figure 13 for both climatologies). As has been stated in Gobiet *et al.* (2005) and is under close investigation at the moment, this measurement bias may mainly be attributed to the ECMWF analyses fields and is probably caused by weak representation of atmospheric wave activity and tropopause height variability. Secondly, the alternating temperature structure with a magnitude of several Kelvin in the southern winter polar vortex region (only visible in JJA 2003) is caused by deficiencies in the representation of the Austral polar vortex in the ECMWF analyses. A detailed analysis can be found in Gobiet *et al.* (2005). Again, with this feature no sampling error is associated.

Our results show that accurate seasonal climatologies between 8 km and 30 km height can be obtained even with data from a single RO receiver. Already now RO based climatologies have the potential to improve modern operational climatologies in regions where the data coverage and/or the vertical resolution and accuracy of RO data is superior to traditional data sources.

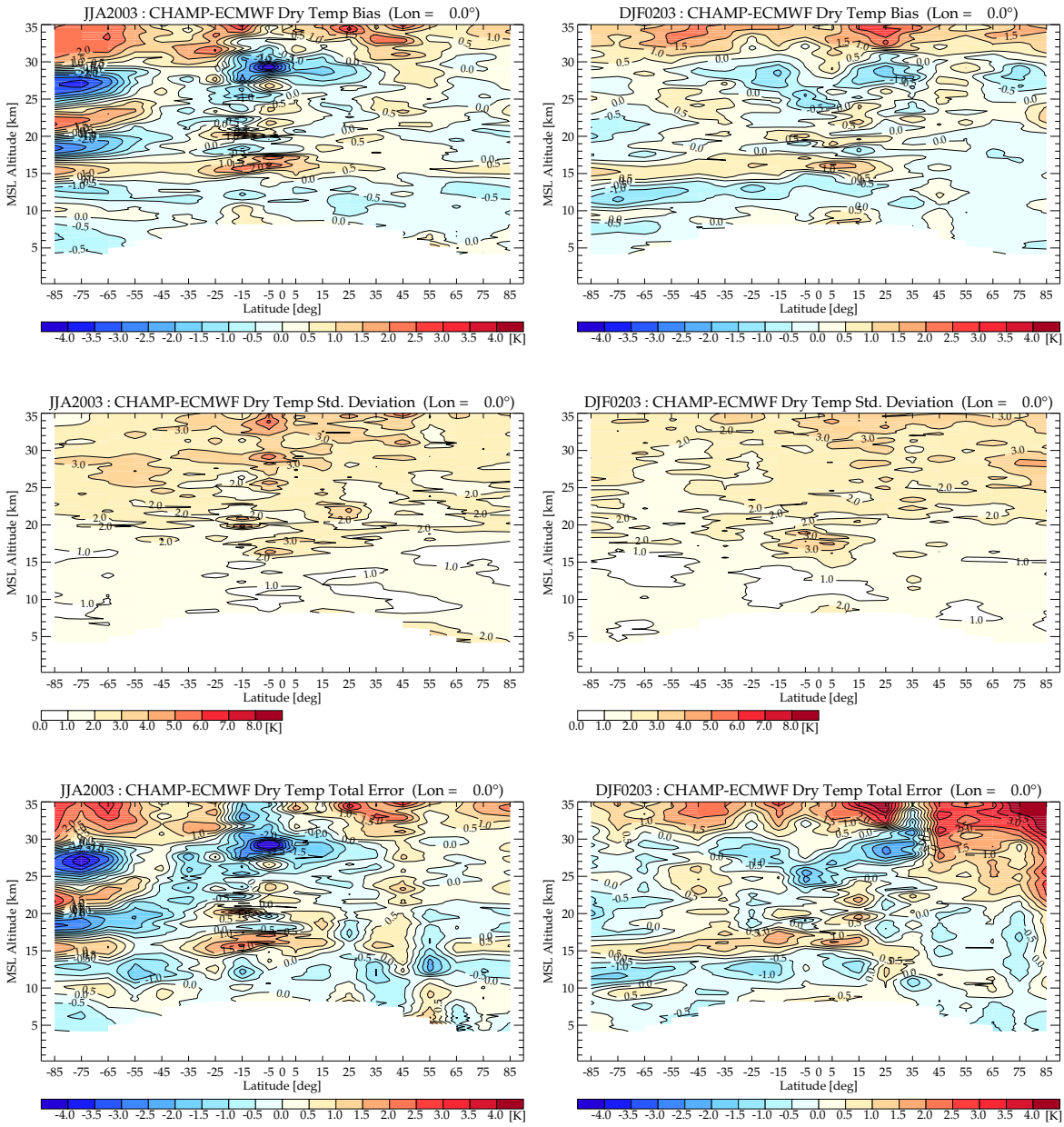

Figure 14: Error fields of CHAMP $10^\circ \times 15^\circ$ gridded climatologies with ECMWF as reference. Season JJA 2003 is shown on the left, DJF 0203 on the right. The error fields comprise from top to bottom: bias (deviation CHAMP-ECMWF), standard deviation, and climatological error.

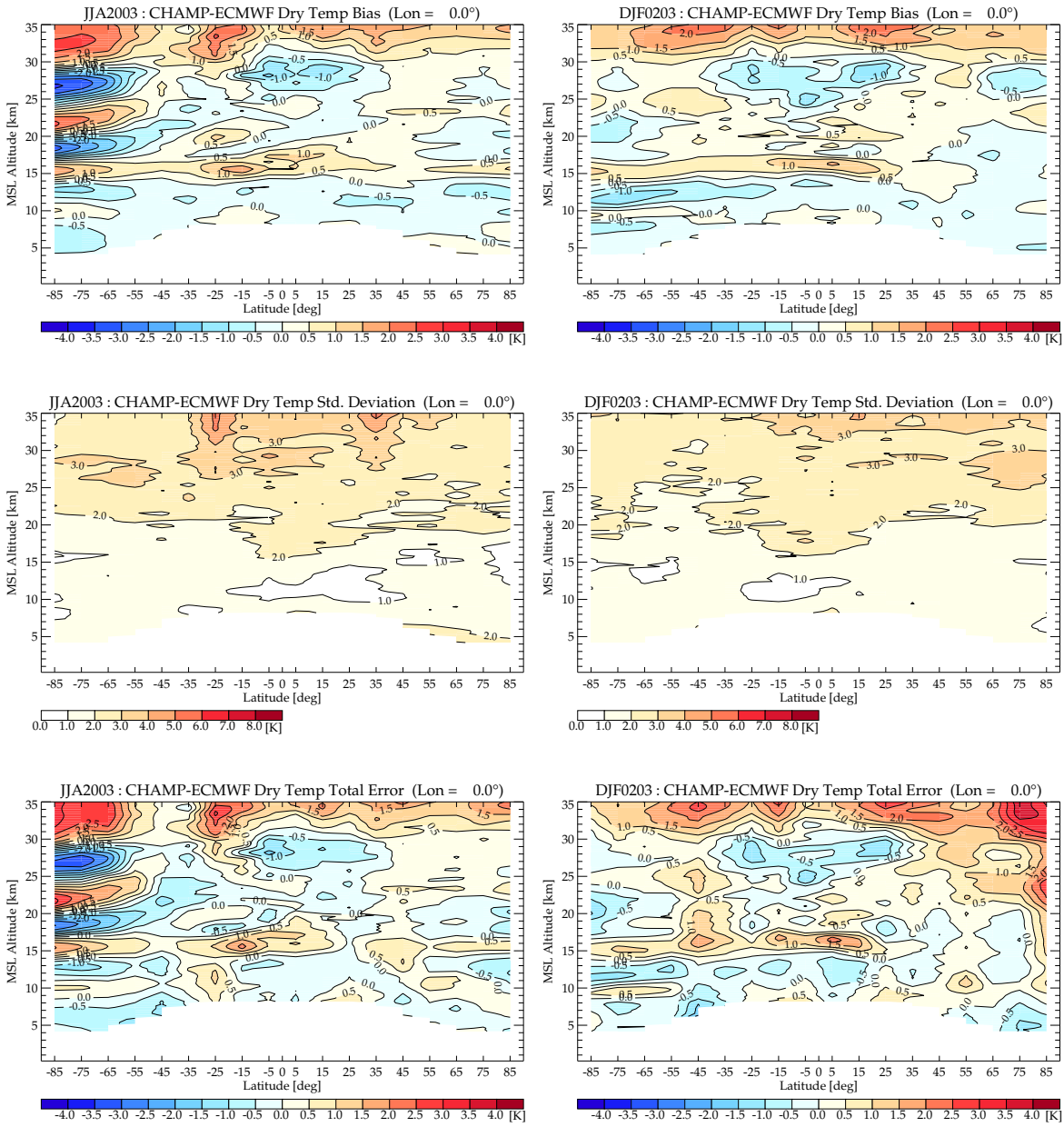

Figure 15: Error fields of CHAMP $10^\circ \times 60^\circ$ gridded climatologies with ECMWF as reference. Season JJA 2003 is shown on the left, season DJF 0203 on the right. The error fields comprise from top to bottom: bias (deviation CHAMP-ECMWF), standard deviation, and climatological error.

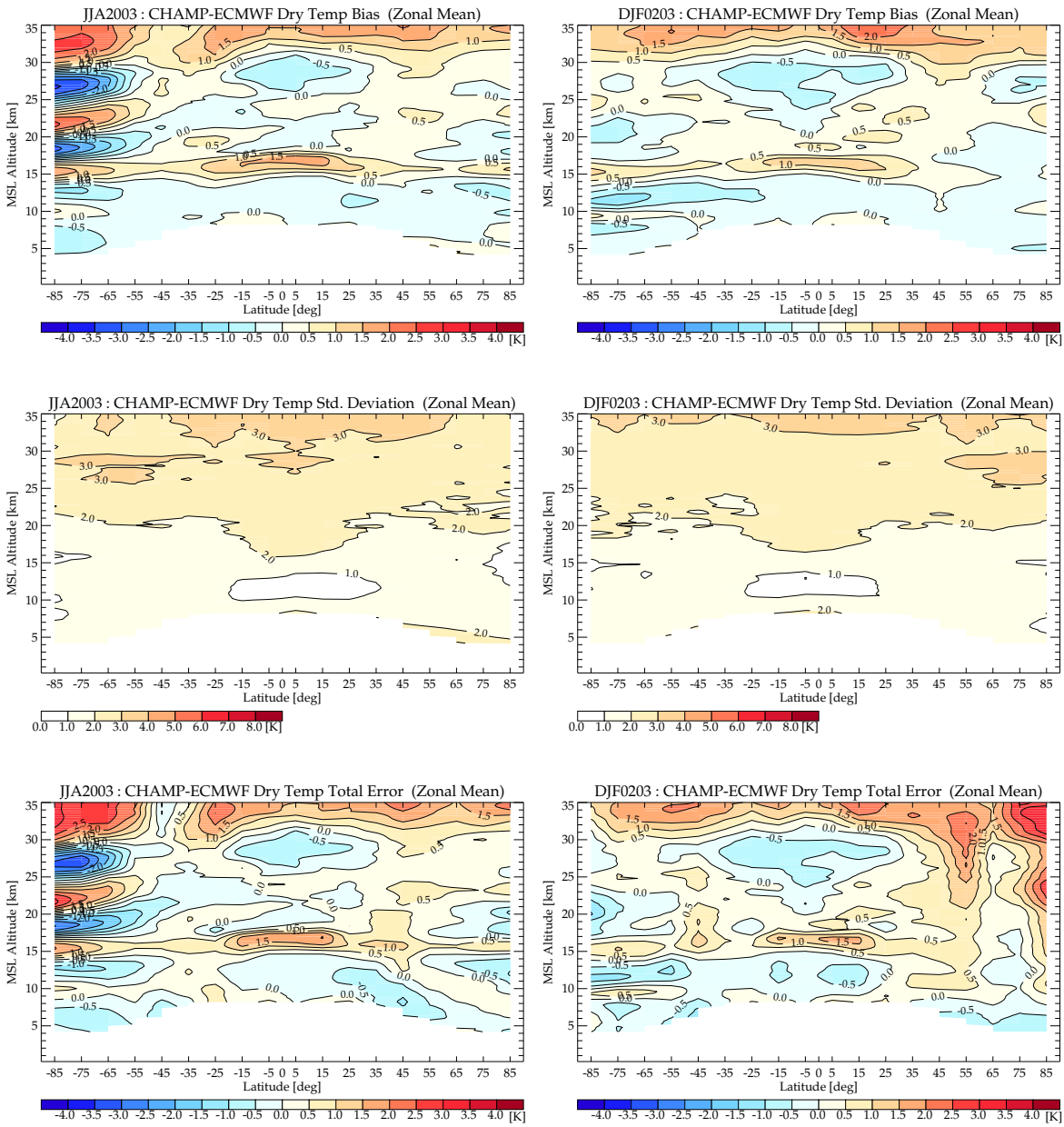

Figure 16: Error fields of CHAMP zonal mean climatologies with ECMWF as reference for JJA 2003 (left) DJF 0203 (right). The error fields comprise from top to bottom: bias (deviation CHAMP-ECMWF), standard deviation, and climatological error.

3 Estimation of Errors Affecting Climatologies

3.1 Estimation of Observational Error based on an Empirical Error Analysis

The assimilation of radio occultation (RO) data has the potential to significantly improve the accuracy of global and regional meteorological analysis and weather prediction, which has been confirmed by several studies (e.g., Kuo *et al.*, 2000; Healy *et al.*, 2005). One important issue in this respect is knowledge of radio occultation measurement errors in order to formulate adequate observation error covariance matrices for data assimilation systems.

Since refractivity seems to be the most appropriate parameter for assimilation purposes (Healy *et al.*, 2005; Syndergaard *et al.*, 2006) we performed an empirical error analysis of a set of refractivity profiles retrieved from CHAMP RO observations. In addition we present results of an empirical error analysis for the parameters pressure, geopotential height, and temperature. Regarding the error analysis method, we build on the heritage of an earlier simulation study (Steiner and Kirchengast, 2004, 2005) and extend it to a separate estimation of the observation error for CHAMP refractivity data.

3.1.1 Description of the Data Set and the Retrieval Scheme

The study is based on a CHAMP level 2 data set comprising two seasons of radio occultation observations, DJF 0203 and JJA 2003. For each season more than 12 000 profiles of atmospheric excess phases were analyzed. The data sets were separated into three latitude bands, low ($-30°$ to $30°$), middle ($\pm 30°$ to $\pm 60°$), and high ($\pm 60°$ to $\pm 90°$) latitudes. In addition, we separately analyzed the Northern Hemispheric (NH) and the Southern Hemispheric (SH) region.

For the basic error study refractivity profiles were processed from the data base of excess phase profiles with the CHAMPCLIM Retrieval version 2.2 (CCRv22), the previous version of CCRv23, including an advanced upper stratospheric retrieval scheme (Gobiet and Kirchengast, 2004b,a). The retrieval is based on the standard geometric optics approach, thus we will not interpret the results below 5 km height. Since the basic study deals with the use of refractivity data for assimilation systems, we used the general MSISE-90 model for the initialization of bending angles. The sample sizes for this refractivity data set (CCRv22, MSISE-90 initialized) are listed in Table 2 which corresponds to Figure 17.

Building on the basic error study design we further analyze errors of refractivity, pressure, geopotenial height, and temperature profiles (Figures 17 to 21) which were processed with the CCRv23 and initialized with ECMWF analysis data at bending angle level. The CCRv23 processing is described in detail in Steiner *et al.* (2004), an overview is given in Borsche *et al.* (2006) as well as in Section 2.1 of this report.

Table 2: The number of occultation events for the different data sets analyzed.

	DJF 0203			**JJA 2003**		
	Total	**NH**	**SH**	**Total**	**NH**	**SH**
Global	12 329	5 995	6 334	12 710	5 989	6 721
Low lat	3 790	1 812	1 978	3 784	1 841	1 943
Mid lat	4 310	2 120	2 190	4 095	1 983	2 112
High lat	4 229	2 063	2 166	4 831	2 165	2 666

3.1.2 Estimation of the Combined Error

The error statistics is based on the comparison of the retrieved and smoothed (comparable to ECMWF vertical grid resolution) refractivity profiles with co-located refractivity profiles derived from 6-hourly operational meteorological analysis fields from ECMWF. The co-located vertical ECMWF profiles were calculated at a fixed mean tangent point location. When regarding the ECMWF profiles as the truth this implies that the error estimates represent an upper bound error estimate including the observation error, the model (ECMWF) error and the representativeness error. The representativeness error stems from the limited spatial and temporal model resolution and from the comparison of the retrieved profiles with vertical reference profiles. This fact becomes important in the troposphere below ~ 7 km, where higher horizontal variability is present (Foelsche and Kirchengast, 2004; Syndergaard *et al.*, 2004). Since we will not interpret results below 5 km, the representativeness errors to this end are largely negligible.

The statistical method for calculating the deviation of CHAMP from ECMWF ($x_{\mathrm{CHAMP}} - x_{\mathrm{ECMWF}}$), denoted as combined error (CHAMP observed error plus ECMWF model error), is described in detail in Steiner and Kirchengast (2004). Bias profiles and error covariance matrices are provided, the latter separated into standard deviation profiles and error correlation matrices.

The resulting error statistics for the combined refractivity error is shown in Figures 17 and 18 with MSIS and ECMWF initialization, respectively. The pressure, geopotential height, and temperature errors based on data initialisation with ECMWF analyses are shown in Figures 19 to 21. These plots represent the global ensemble and the latitudinal data sets (horizontal panel rows), globally (left), for the Northern Hemisphere (middle), and the Southern Hemisphere (right) up to 35 km height for the JJA 2003 season (solid) and for the DJF 0203 season (dashed). For refractivity and pressure the relative bias (green) and the relative standard deviation (Rel.StdDev) (black) of CHAMP RO with respect to ECMWF are shown, whereas for geopotential height and temperature the absolute bias (green) and absolute standard deviation (black) are shown.

In Figure 17 the relative refractivity bias of CHAMP RO with respect to ECMWF oscillates around $-0.4\,\%$ at 5 km to 25 km globally as well as at mid- and high latitudes, increasing to $0.5\,\%$ to $1\,\%$ at 35 km. Bias oscillations are seen at low latitudes, ranging from $-0.4\,\%$ to $0.5\,\%$ at 5 km to 35 km with salient structures appearing at tropopause heights. This effect may partly be due to the higher resolved tropopause in CHAMP RO data than in ECMWF data (RO resolution ~ 1 km at that altitude, ECMWF analyses > 1.3 km) but may also stem from a weak representation of tropopause height variability in the ECMWF analysis fields (Gobiet *et al.*, 2005). The most prominent features can be seen in SH winter at high latitudes (lower left panel), which is an indication that the ECMWF field does not accurately represent the polar vortex in this region (Gobiet *et al.*, 2005). The smallest bias occurs at NH high latitudes (lower middle panel) being $-0.3\,\%$ at 5 km to 25 km in DJF 0203 almost vanishing in JJA 2003.

The combined Rel.StdDev is of the order of $0.7\,\%$ to $1\,\%$ at 5 km to 28 km height globally and at low latitudes (NH and SH). At mid- and high latitudes the Rel.StdDev shows different behavior in the winter hemisphere and in the summer hemisphere at upper stratospheric heights, being $0.75\,\%$ to $1\,\%$ at 20 km to 34 km in summer becoming twice as large ($\sim 2\,\%$ at 35 km) in winter. This may partly be due to the larger atmospheric variability in winter and is subject to further investigation.

Figure 18 shows the combined refractivity error as a function of MSL altitude. Basically the same features are prominent as in Figure 17. The main difference is that the relative refractivity bias stabilizes above 25 km due to the ECMWF background data used in the initialization. The bias oscillates around $-0.3\,\%$ globally and around $-0.4\,\%$ at middle latitudes at 5 km to 35 km.

The combined Rel.StdDev is of the order of $0.6\,\%$ to $1\,\%$ at 5 km to 35 km altitude globally and at low latitudes (NH and SH). At mid- and high latitudes the Rel.StdDev shows a similar

but not as marked behavior as in Figure 17 regarding the differences in the winter hemisphere and in the summer hemisphere. In the summer hemisphere the combined Rel.StdDev is of the order of 0.6 % to 0.7 % at 5 km to 26 km increasing to 1 % (1.5 %) at 30 km (35 km) altitude. In winter above 20 km altitude the Rel.StdDev increases to 1 % at about 25 km, up to 1.5 % (1.9 %) at 35 km at mid-latitudes (high latitudes).

Figure 19 shows the combined pressure error as a function of MSL altitude. The relative bias increases from 0 at 5km to −0.3 % (−0.4 %) at 15 km, then decreases to about −0.1 % at 30 km altitude for the global (mid-latitude) data set. At high latitudes the relative bias is of the order of −0.3 % between 7 km and 31 km, showing a twice as large difference between NH winter and NH summer, and the above discussed oscillating structure in SH winter. The relative bias at low latitudes is about 0.3 % at 5 km changing to −0.3 % at 15 km and keeping constant at about 0.2 % above 16 km altitude.

The Rel.StdDev shows the same structure for the global and the latitudinal data sets above about 10 km altitudes. It is about 0.3 % between 10 km and 15 km increasing to 1 % at 26 km and to 1.7 % at 35 km altitude. At high latitudes a larger difference between summer and winter is visible above 15 km altitude. In tropospheric altitudes differences occur with a Rel.StdDev of 0.4 % at high latitudes, of 0.6 % globally and at mid-latitudes, and of 1 % at low latitudes at 5 km altitude. The seasonal differences at tropospheric altitudes are most pronounced in low latitude.

Figure 20 shows the combined geopotential height error as a function of pressure altitude in form of absolute bias and absolute standard deviation (StdDev). The overall structure of bias and StdDev are the same as for the pressure error discussed in Figure 19 above.

For the global data set the bias is of the order of 20 gpm (geopotential meters) above 8 km altitude. At low latitudes the bias extends to about 20 gpm at upper tropospheric/lower stratospheric heights, almost vanishing above 17 km altitude. At mid-latitudes the bias increases from 0 at 5 km altitude to 30 gpm between 10 km to 15 km altitude, then decreasing to 20 gpm at 25 km and to 0 at 35 km altitude. The high latitudes show a bias of about 20 gpm to 30 gpm above 8 km altitude.

The StdDev is of the order of 20 gpm between about 8 km to 15 km increasing to 50 gpm at 25 km and to 110 gpm at 35 km altitude. As for pressure small latitudinal differences at tropospheric heights are seen which range from 25 gpm at high latitudes to 50 gpm at low latitudes at 5 km altitude. The differences in upper stratospheric heights regarding winter and summer are not as marked as for pressure.

Figure 21 depicts the temperature error statistics based on difference profiles which are determined by substracting IGAM/ECMWF retrieved temperatures from ECMWF co-located temperature profiles. The temperature bias of CHAMP RO with repect to ECMWF oscillates globally around 0 K at 5 km to 30 km, the oscillation stemming mainly from the prominent features in SH winter at high latitudes due to the inaccurate representation of the polar vortex in ECMWF analyses (see explanation above). Another significant error feature can be seen in low latitudes at tropopause height with a temperature bias of the order of 1.5 K (confer Section 2.3).

The standard deviation for the global data set amounts to 2 K at 5 km and to ∼1 K at 8 km to 15 km increasing to 2 K at 25 km and to 2.5 K at 35 km. At mid latitudes the 1-K range extends from 8 km to 17 km, up to 28 km the standard deviation amounts to 1.5 K. The standard deviation at low latitudes amounts to 3 K at 5 km decreasing to 0.8 K between 8 km and 14 km, then increasing to 2 K at 25 km and to 2.8 K at 35 km. The high latitudes globally show a standard deviation of 1 K between 7 km and 17 km increasing to 2 K at 25 km. Here, the standard deviation above 20 km is bigger in the winter season than in the summer season. Except for high latitudes no significant seasonal difference to the standard deviation occurs.

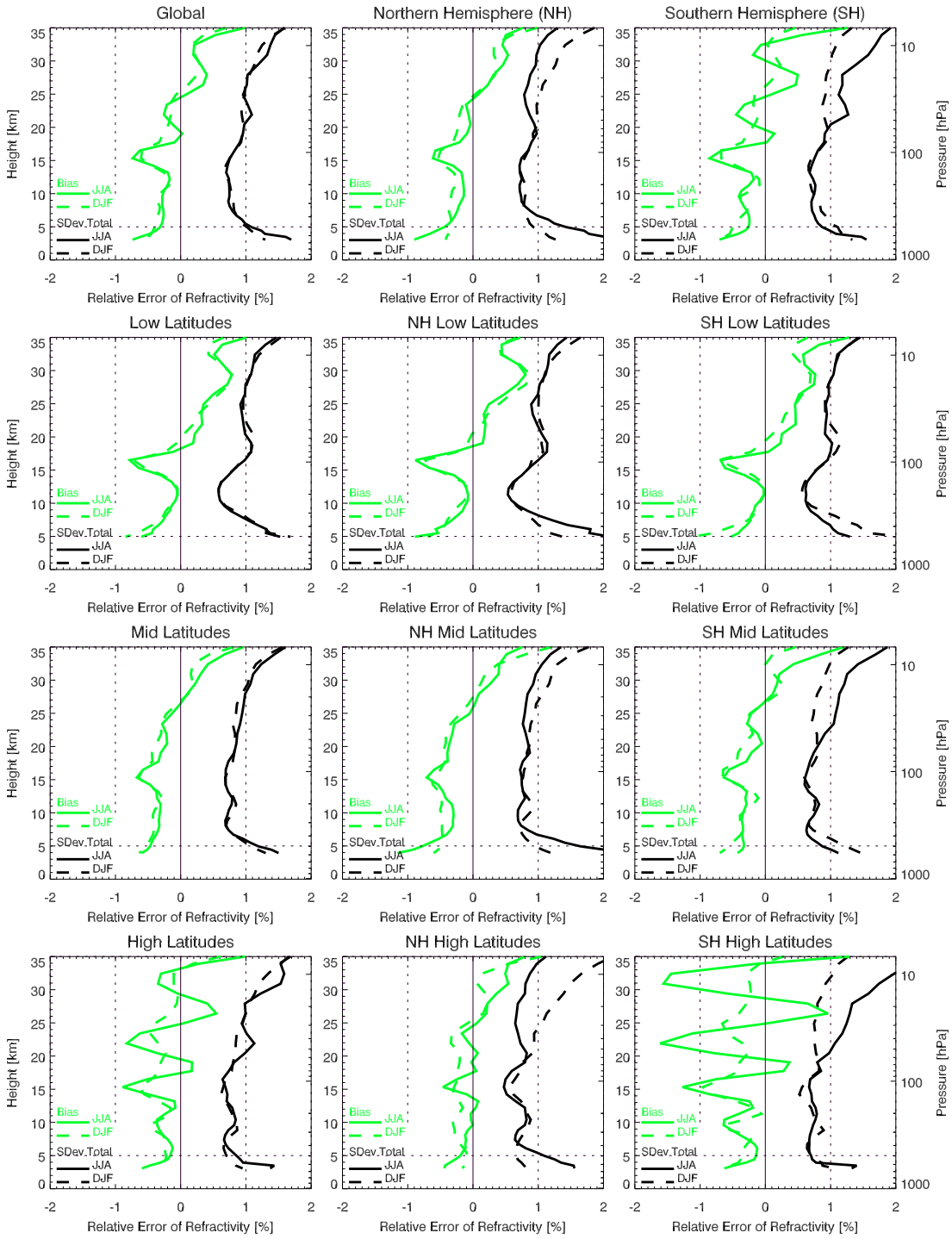

Figure 17: Combined refractivity error as a function of height for the global and the latitudinal ensembles (horizontal panel rows), globally (left), Northern Hemisphere (middle), Southern Hemisphere (right). Relative bias (green) and relative standard deviation (black) are shown for the JJA 2003 season (solid) and for the DJF 0203 season (dashed), respectively. The refractivity retrieval (CCRv23) in this case is based on data initialization with MSISE–90 climatology.

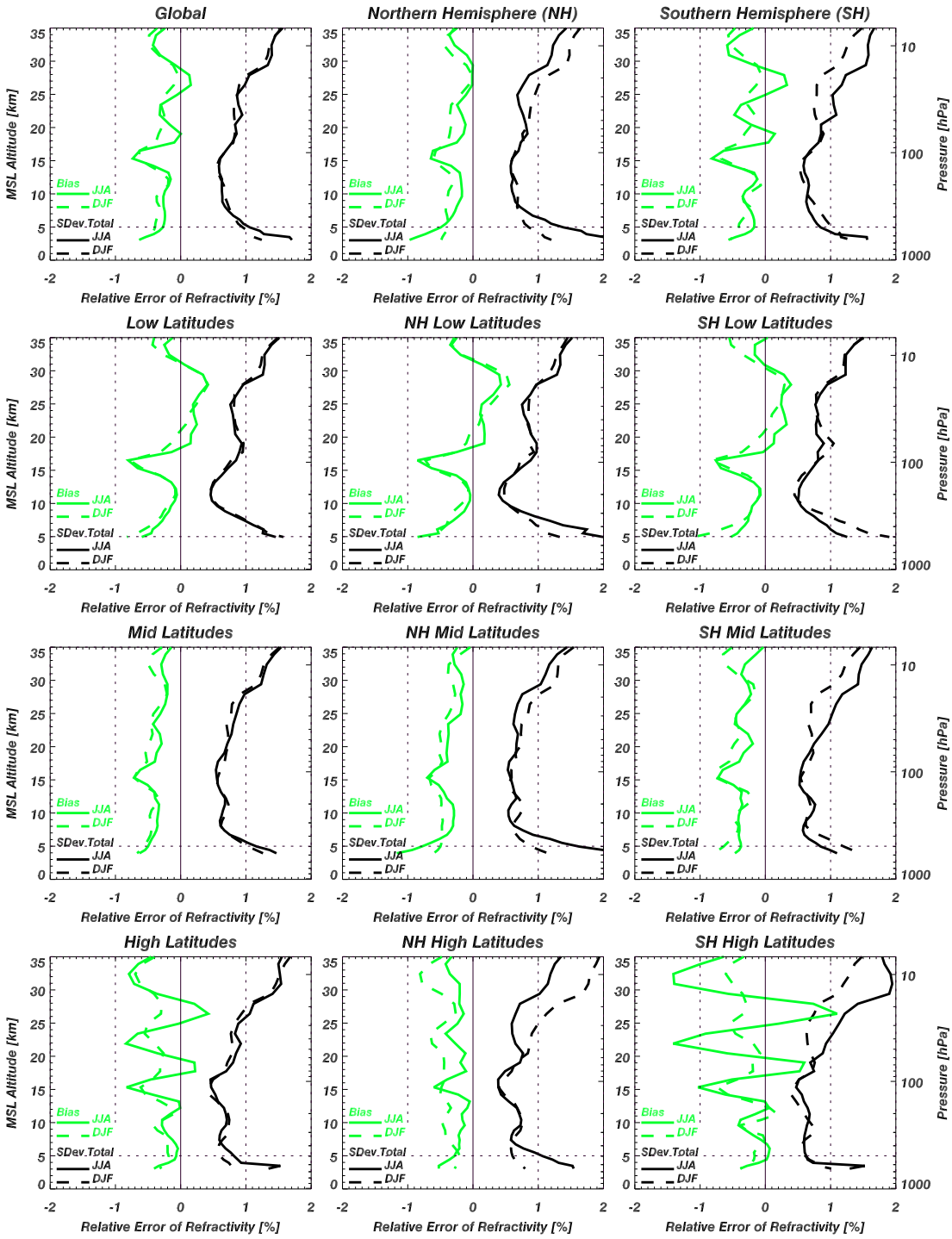

Figure 18: Combined refractivity error as a function of MSL altitude, the refractivity retrieval (CCRv23) in this case is based on data initialization with ECMWF operational analysis fields. Figure layout and style same as Figure 17, see that caption for details.

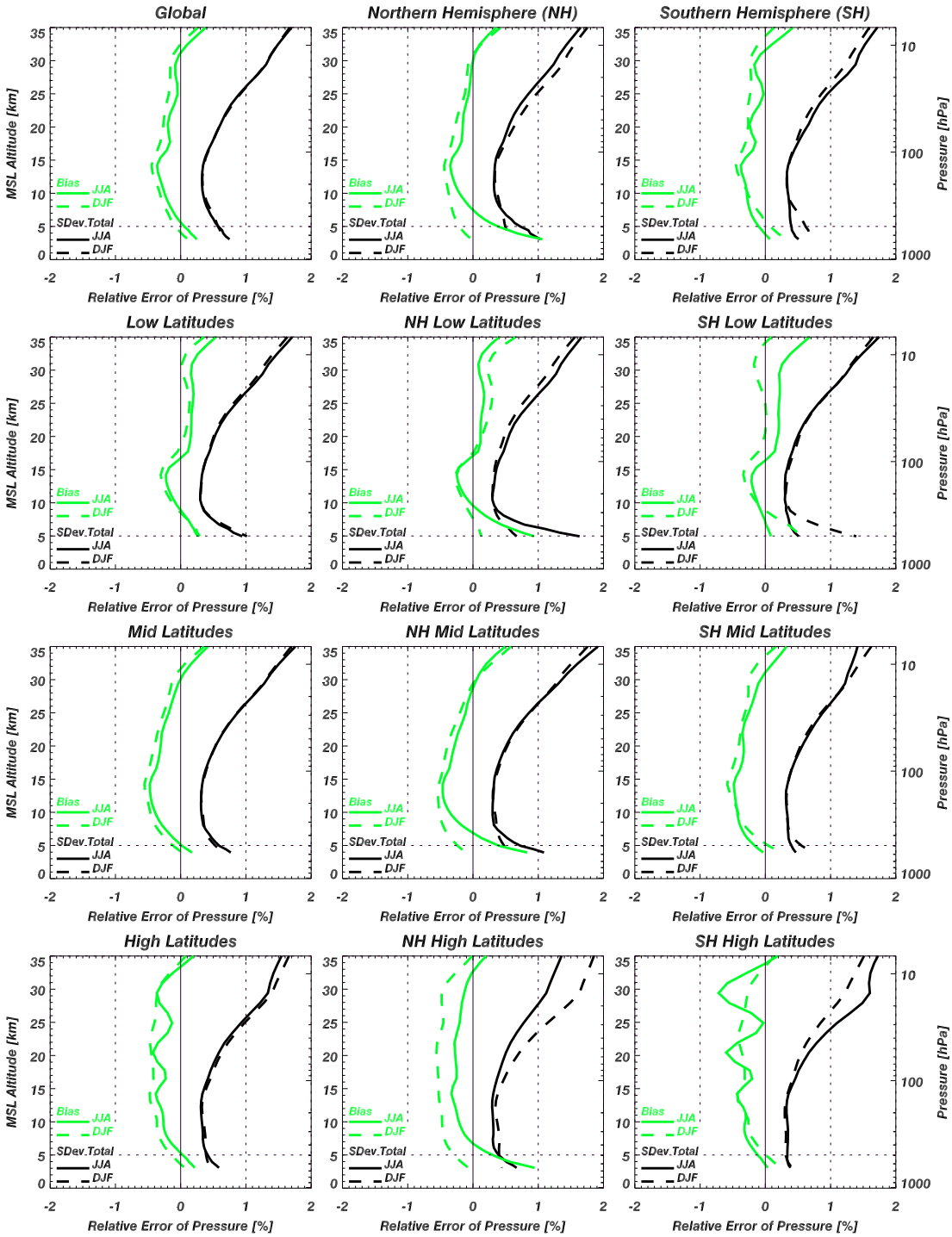

Figure 19: Combined pressure error as a function of MSL altitude, the retrieval (CCRv23) is based on data initialization with ECMWF operational analysis fields. Relative bias (green) and relative standard deviation (black) shown for the JJA 2003 season (solid) and for the DJF 0203 season (dashed), respectively. Figure layout same as Figure 17, see that caption for details.

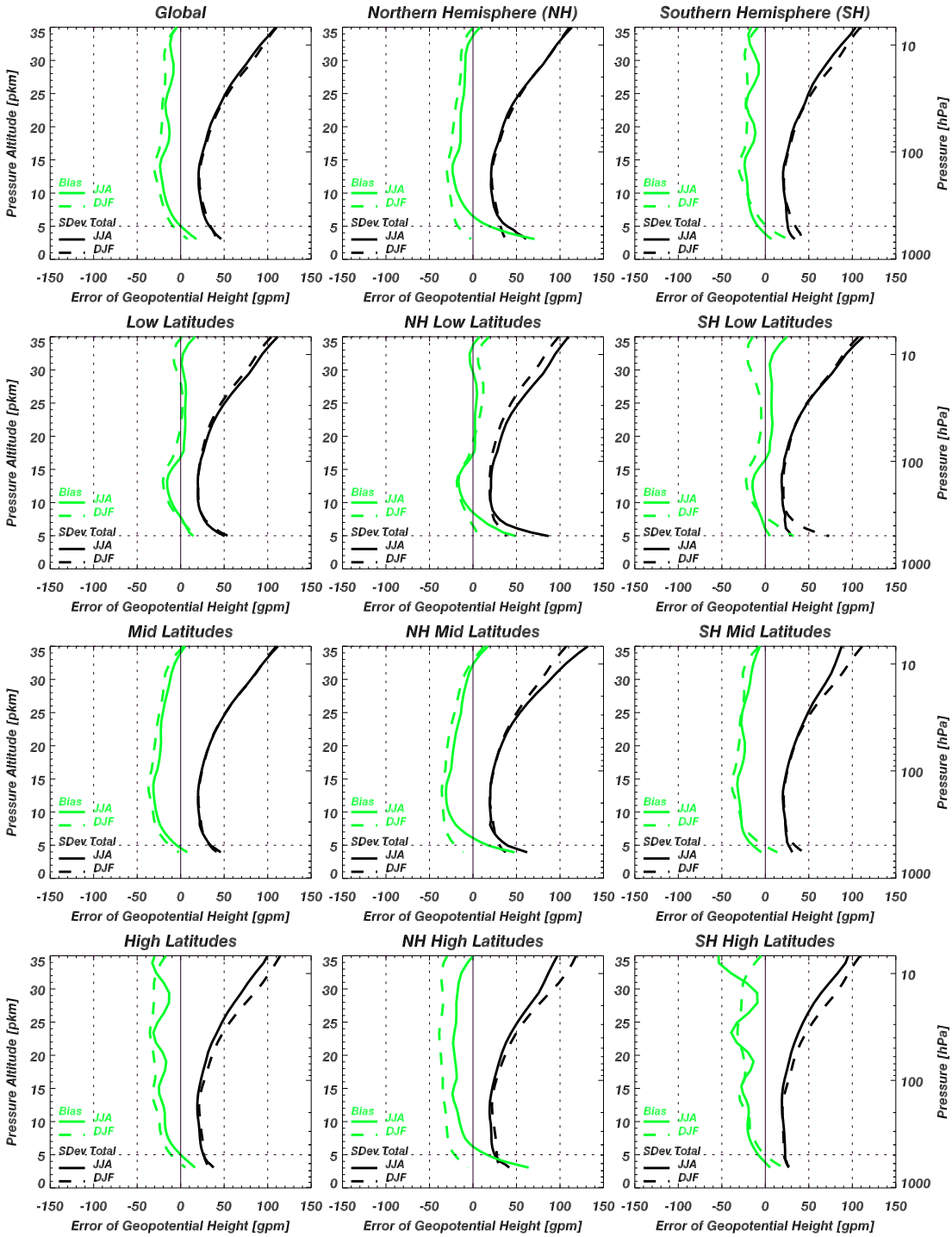

Figure 20: Combined geopotential height error as a function of pressure altitude, the retrieval (CCRv23) is based on data initialization with ECMWF operational analysis fields. Absolute bias (green) and absolute standard deviation (black) are shown for the JJA 2003 season (solid) and for the DJF 0203 season (dashed), respectively. Global and latitudinal ensembles (horizontal panel rows) are shown, globally (left), Northern Hemisphere (middle), Southern Hemisphere (right).

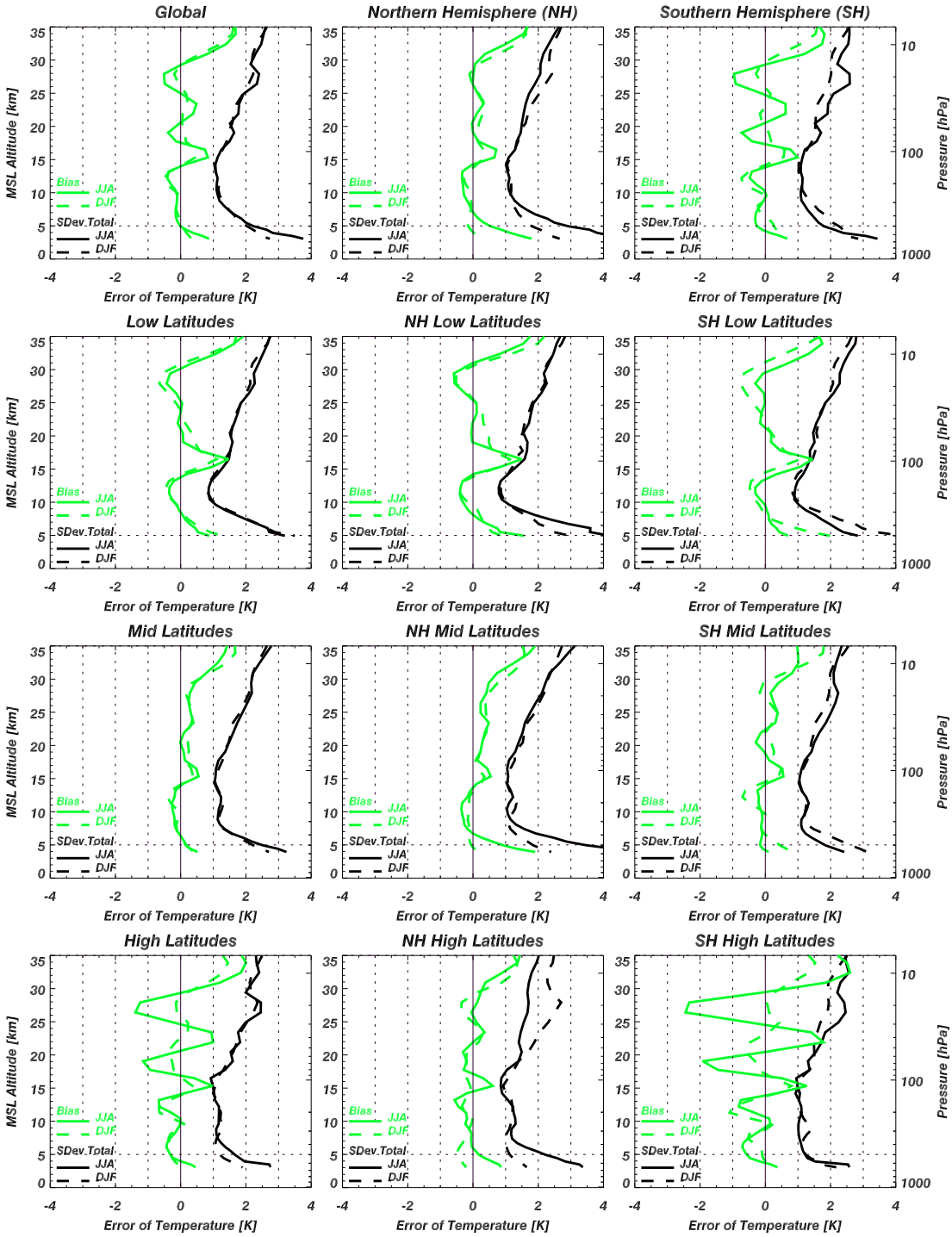

Figure 21: Combined temperature error as a function of MSL altitude for the global and the latitudinal ensembles (horizontal panel rows), globally (left), Northern Hemisphere (middle), Southern Hemisphere (right). Bias (green) and standard deviation (black) are shown for the JJA 2003 season (solid) and for the DJF 0203 season (dashed), respectively. The retrieval (CCRv23) is based on data initialization with ECMWF operational analysis fields.

3.1.3 Estimation of the ECMWF Error

In order to separate the observed error of the CHAMP RO refractivity retrievals from the combined error, we calculated a global estimate of the ECMWF refractivity model error. M. Fisher (ECMWF, Reading, U.K., pers. communications, 2004) provided global error estimates of ECMWF analyses in form of standard deviations for temperature, specific humidity, and surface pressure, and of vertical error correlations for temperature and specific humidity. Temperature T [K], water vapor pressure e [hPa], and total pressure p [hPa] are related to refractivity N [N units] via the Smith-Weintraub formula (Smith and Weintraub, 1953),

$$N = c_1 \frac{p}{T} + c_2 \frac{e}{T^2} \tag{1}$$

with the constants c_1 =77.6 K/hPa and c_2 =3.73·10^5 K^2/hPa. Water vapor pressure in Equation 1 was substituted for specific humidity q [kg/kg] using the following relation,

$$e = \frac{p \cdot q}{a + b\,q} \tag{2}$$

with a =0.622 and b =0.378. A simple error propagation based on Equation 1 was applied via

$$\Delta N = \sqrt{\left(\frac{\partial N}{\partial T}\Delta T\right)^2 + \left(\frac{\partial N}{\partial q}\Delta q\right)^2 + \left(\frac{\partial N}{\partial p}\Delta p\right)^2} \tag{3}$$

in order to calculate the standard deviation of refractivity. The pressure error at a given height was calculated by error propagation using the given standard deviation of surface pressure of 2.5 hPa. The vertical refractivity error correlations were derived by a weighted combination of temperature error correlations ($w_T = \Delta N(\Delta p, \Delta T)/\Delta N(\Delta p, \Delta q, \Delta T)$) and specific humidity error correlations ($w_q = \Delta N(\Delta q)/\Delta N(\Delta p, \Delta q, \Delta T)$).

Figure 22 displays global ECMWF error specifications for temperature (left panels), specific humidity (middle panels), and estimated refractivity (right panels). Standard deviations are shown in the upper panel row and error correlation functions for three different height levels ($\sim$10 km, $\sim$20 km, $\sim$30 km for T and N; $\sim$3 km, $\sim$6 km, $\sim$10 km for q) are presented in the lower panel row.

We tested the sensitivity of the estimated refractivity error with respect to the temperature error input for the four cases displayed in Figure 22, where we multiplied the temperature standard deviation (case 1×T in blue) by 1.5 (green), 2 (red), and 2.5 (black). The results judged most reasonable were found for the case of doubling the temperature standard deviation (2×T case), giving a Rel.StdDev of ECMWF refractivity of the order of 0.5 % at 8 km to 15 km increasing to 0.75 % at 30 km and to 1 % at 35 km. These results are consistent with the findings of Kuo *et al.* (2004) who performed an estimation of short-range forecast errors using the Hollingsworth-Lönnberg method (Hollingsworth and Lönnberg, 1986). For comparison we included their estimates for low latitudes (dotted) and mid-latitudes (dashed) in Figure 22 (upper right panel).

3.1.4 Estimation of the Observation Error

The observed refractivity error was then derived by subtracting the ECMWF error from the combined error in terms of variances s^2,

$$s^2_{\text{Obs}} = s^2_{\text{combined}} - s^2_{\text{ECMWF}} \tag{4}$$

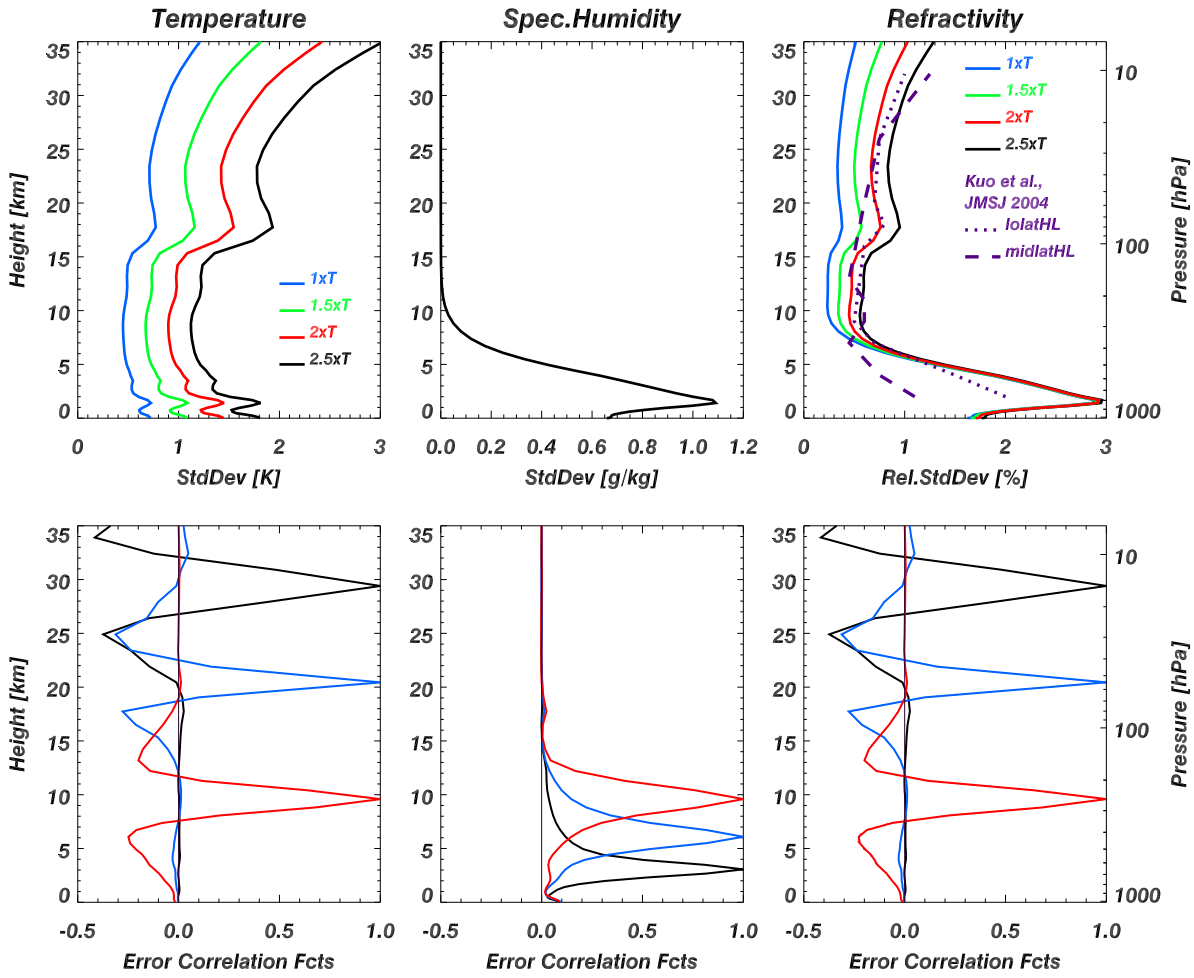

Figure 22: ECMWF error for temperature (left) for 4 test cases ($1 \times T$, $1.5 \times T$, $2 \times T$, $2.5 \times T$), specific humidity (middle), and corresponding estimated refractivity (right) in terms of standard deviation (upper panels) and error correlation functions (lower panels), the latter shown for three heights ($\sim$10 km (red), $\sim$20 km/humidity: 6 km (blue), $\sim$30 km/humidity: 3 km (black)). Estimates of short-range forecast errors for refractivity for low latitudes (dotted) and mid-latitudes (dashed) made in Kuo *et al.* (2004) are also shown (upper right panel).

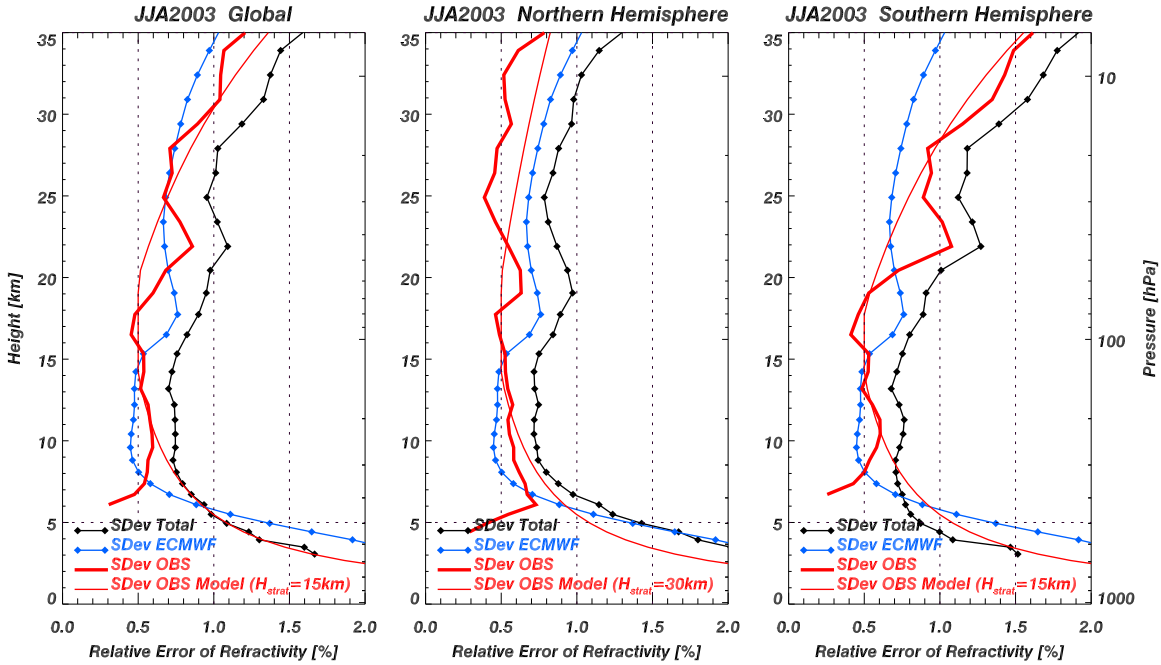

Figure 23: Rel.StDev of refractivity for JJA 2003: combined (black diamond shaped symbols), ECMWF (blue diamond shaped symbols), observed (red thick), model (red thin); global (left), NH (middle), SH (right).

The results are displayed in Figure 23 for the JJA 2003 season showing the combined error (black with diamond symbols), the ECMWF error for the $2\times T$ case (blue), and the corresponding observation error (red) in terms of Rel.StdDev, respectively.

The corresponding global estimate of the observed Rel.StdDev for CHAMP refractivity ($2\times T$ case) is of the order of 0.5 % at 6 km to 18 km, increasing to 0.7 % at 28 km and to 1.2 % at 35 km (left panel). At upper stratospheric heights the observed Rel.StdDev is around 0.5 % at 10 km to 32 km in summer (middle panel) whilst it reaches 1 % to 1.5 % in winter. Our observation error appears to be a more conservative estimate compared to the results of Kuo *et al.* (2004), who found the observation error of refractivity to be of the order of 0.3 % to 0.5 % at 5 km to 25 km.

As a further result, refractivity error correlation functions are displayed in Figure 24 for three different heights, $\sim$10 km, $\sim$20 km, $\sim$30 km, representative for the troposphere, the lower, and the upper stratosphere, respectively. Basically, these functions express the correlation of errors at these heights with the errors in the remainder of the profile. The ECMWF refractivity error correlation functions (dotted) show negative correlation features in the vicinity of the peaks whilst the correlation functions for the combined error (solid with diamond shaped symbols) show a flattening. These features suggest that the correlation wings are dominated by the observed data.

For the construction of refractivity observation error covariance matrices for data assimilation systems we therefore suggest a combination of the observed Rel.StdDev with the total error correlation matrix. We provide simple analytical formulations of refractivity error covariance matrices, which were deduced in a simulation study for a Metop/GRAS receiving system (Steiner and Kirchengast, 2005). The functional formulations for Rel.StdDev and for correlation functions depend on a few parameters, which can be fitted for any given data set. Table 3 summarizes the functions. Using them for Rel.StdDev and approximating an exponential drop-off for the error correlations, a simple covariance matrix model S for the observed refractivity error can then be

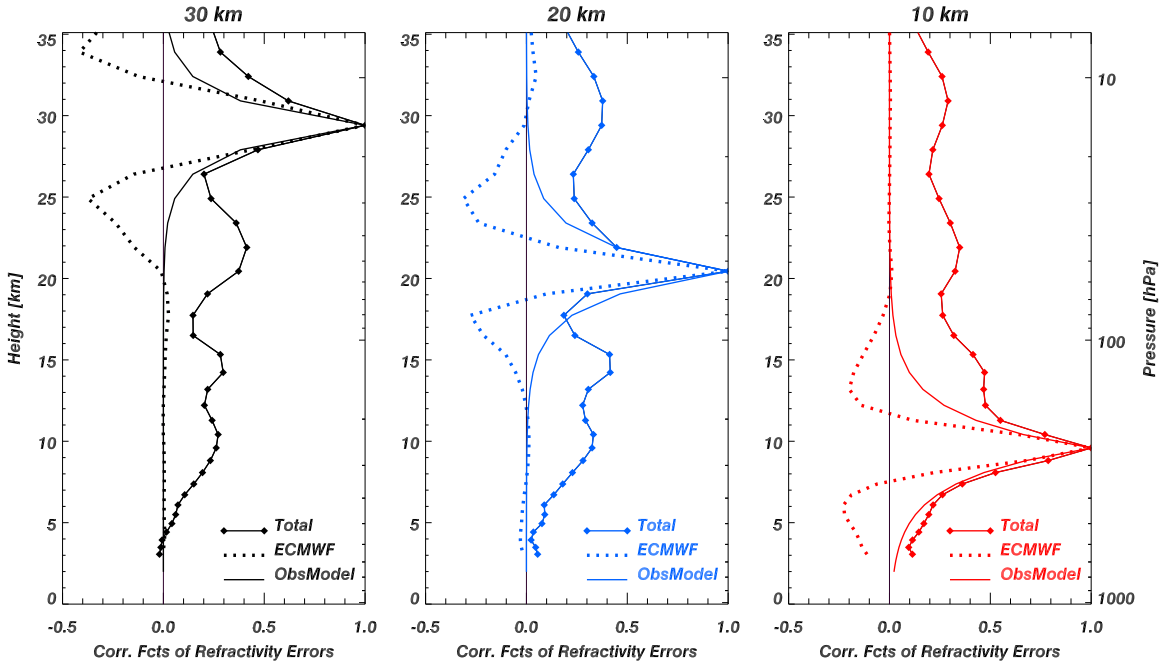

Figure 24: Error correlation functions for the refractivity error: combined (solid line with diamond shaped symbols), ECMWF (dotted), and analytical exponential drop-off model (solid) shown for three heights ∼30 km (black), ∼20 km (blue), ∼10 km (red).

constructed via

$$\mathsf{S} = s_i s_j \exp(-|z_i - z_j/L(z)|) \tag{5}$$

Figure 23 visualizes the analytical functions (thin solid) for the observed Rel.StdDev (thick solid) for the JJA 2003 season; Figure 24 those for the error correlation (thin solid). In order to fit the seasonal behavior of the Rel.StdDev we adjusted the scale height of error H_{strat} to 30 km for summer (NH) and the bottom level of the stratosphere domain z_{stratbot} to 18 km for winter (SH). The validity of the fit regarding the upper height limit depends on the receiving system, e.g., 35 km for CHAMP data and 50 km for Metop/GRAS (Steiner and Kirchengast, 2005).

3.2 Sampling Error due to Local Time Distribution

In the horizontal, the spatial measurement density depends on the temporal averaging period and on geometrical properties of the measurement system. In case of CHAMPCLIM, one GPS receiver on a LEO satellite with high orbital inclination yields some 150 globally well distributed atmospheric profiles per day with higher density (referred to equal areas) at high latitudes and lower density at low latitudes (confer Section 2.2.2).

Additionally, it is of interest to evenly sample the diurnal cycle. According to the orbit parameters of CHAMP, the local time of the ascending and descending nodes is at about the same time as the local time of the corresponding occultation events. With a change rate of ∼1 hour per 11 days of both nodes the diurnal cycle is ideally scanned within ∼130 days. This implies that even seasonal means (90-92 day period) are not ideally sampling the diurnal cycle.

The lack of continuity in the coverage, leading to sampling error, is a characteristic problem of (low earth-orbiting) satellite data. In terms of temperature data retrievals, the local time of the occultation events plays an essential role because of distinct daily temperature variations. A

Table 3: Rel.StdDev s(z) model for CHAMP refractivity with respective fitting parameters: z_{troptop} denoting the top level of the "troposphere domain", z_{stratbot} the bottom level of the "stratosphere domain", s_{utls} the Rel.StdDev between z_{troptop} and z_{stratbot}, s_0 the best-fit value for the Rel.StdDev at ∼1 km, H_{strat} the scale height of error, and $L(z)$ the correlation length, respectively.

	Relative Standard Deviation $s(z)$		**Correlation Length $L(z)$**
$\mathbf{2\,km < z \leq z_{troptop}}$	$s_{\text{utls}} + s_0(1\,\text{km}/z - 1\,\text{km}/z_{\text{troptop}})$	$s_{\text{utls}} = 0.5\,\%$ $s_0 = 4.5\,\%$	$L = 2\,\text{km}$
$\mathbf{z_{troptop} < z < z_{stratbot}}$	s_{utls}	$z_{\text{troptop}} = 14\,\text{km}$ global/NH: $z_{\text{stratbot}} = 20\,\text{km}$ SH: $z_{\text{stratbot}} = 18\,\text{km}$ global/SH: $H_{\text{strat}} = 15\,\text{km}$ NH: $H_{\text{strat}} = 30\,\text{km}$	linear decrease to $L = 1\,\text{km}$ at $z = 50\,\text{km}$
$\mathbf{z_{stratbot} \leq z < 35\,km}$	$s_{\text{utls}} \exp\left[(z - z_{\text{stratbot}})/H_{\text{strat}}\right]$		

monthly shift of the local time of a certain (meridional) sector's occultation events could dupe a temperature trend without physical relevance – simply caused by an inappropriate sampling interval. To explore the retrieved data behavior, the local time for each event (in units [hrs], longitude λ in units [deg]) was calculated:

$$\text{LocalTime}_{\text{event}} = \text{UTC}_{\text{event}} + \lambda_{\text{event}} \cdot \frac{24\,\text{hrs}}{360^\circ} \tag{6}$$

3.2.1 Investigation of Monthly Local Time Distribution

To get an impression of the local time distribution of RO events, for the summer months June, July, and August 2003 the local times for the profiles of each month were plotted depending on the longitude of the events as shown on the left side of Figure 25. The graphs show that the events are not uniformly distributed in time but tend to accumulate "twofold" during a month with a time lag of roughly twelve hours in between. The time range of the event accumulation varies about three hours from month to month, as can clearly be seen from the histograms on the right side of Figure 25. While in June 2003 the peaks of the bimodal distribution of the histogram occur around midnight (between 12 p.m. and 3 a.m.) and noon (12 a.m. to 3 p.m.), while one month later in July 2003 the peaks move to late morning (between 9 a.m. to 12 a.m.) and late evening (between 9 p.m. to 12 p.m.). This scheme applies to the remaining months as well.

3.2.2 Investigation of Seasonal Local Time Distribution

As expected, the local time influence fades when seasons are considered instead of months. In Figure 26 on the left side the better (although not yet "perfect") event distribution is shown for the seasons DJF 0203 and JJA 2003 at the top and at the bottom, respectively. On the right side, the histograms are shown in which two narrow gaps remain, while two broad peaks were formed. The error contribution of the uneven local time sampling is still under investigation, preliminary results, however, show that it is small compared to the general spatial sampling error.

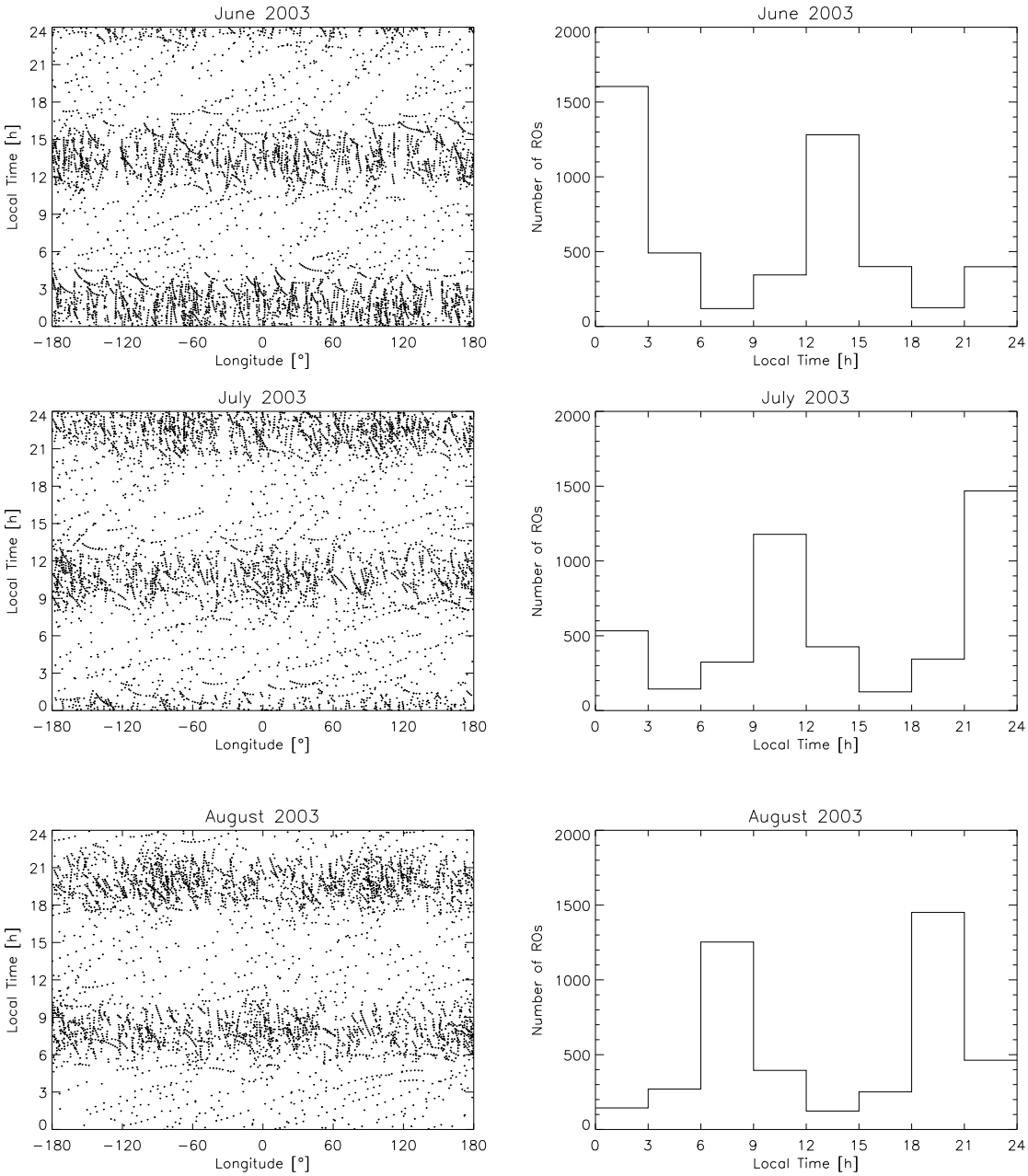

Figure 25: Local time distribution of RO events June – August 2003. On the left hand side: Local time of radio occultation events as a function of longitude. On the right hand side: Histogram of number of radio occultation events within three hour time intervals. A time shift of approximately three hours per month is clearly visible.

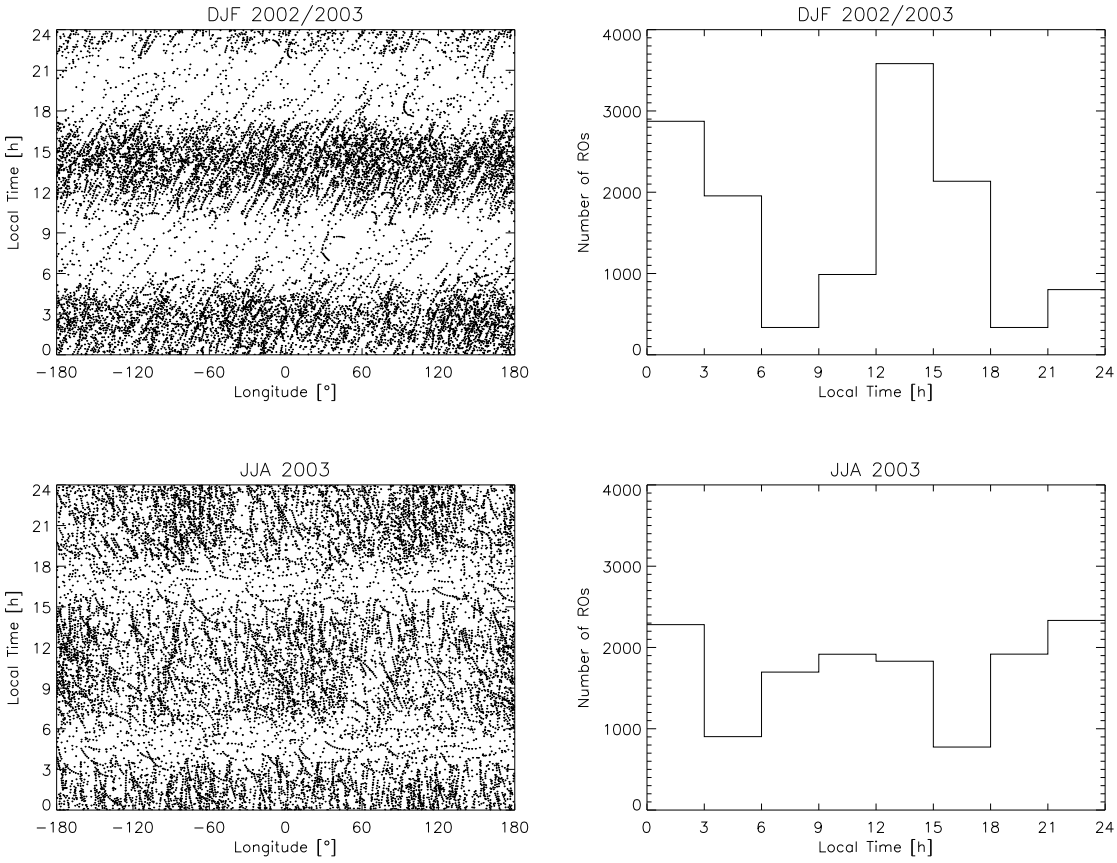

Figure 26: Local time distribution of RO events for the DJF 0203 and JJA 2003 seasons. On the left: Local time of radio occultation events as a function of longitude. On the right: Histogram of number of radio occultation events within three hour time intervals.

4 Conclusions and Outook

This report from the second phase of the CHAMPCLIM project (CHAMPCLIM-2) presented work on establishing a pre-operational retrieval and processing system for creating RO based climatologies. Whereas the first part CHAMPCLIM-1 has achieved sufficiently validated data processed by sufficiently advanced algorithmic chains, CHAMPCLIM-2 concentrated on creating month-to-month, season-to-season, and year-to-year climatologies in a pre-operational way.

The algorithm for retrieving the CHAMP profiles has been modified by adding the calculation of tropopause parameters including the lapse rate tropopause height and temperature and the cold point tropopause height and temperature. Results have been shown, which demonstrate the feasibility of the algorithm applied to the CHAMP data. Furthermore, the CHAMP data were referenced to the geoid instead of the reference ellipsoid according to the specification of the ECMWF reference data. Even though the effect is small and does hardly show up in zonal mean temperature climatologies, by doing so a systematic improvement was brought to the retrieval algorithm. As has been shown, the difference in temperature in special latitude slices may reach up to 0.6 K. Parameters with exponential height variation, such as refractivity and pressure, receive more marked improvement.

It is an indispensable prerequisite for the creation of RO based climatologies to first validate the measurements as done in the CHAMPCLIM-1 part and then to determine the error of the measurement. We presented an error analysis for CHAMP RO refractivity profiles, processed with the WegCenter CCRv23 scheme, for two seasons, DJF 2002/03 and JJA 2003. The error statistics were based on a comparison to reference profiles from ECMWF analysis fields, implying that the statistics include both, the observation error and the ECMWF model error. In order to separate the errors we performed an error estimation of the ECMWF error based on error propagation of temperature, humidity, and pressure error into refractivity error. Finally, the subtraction of the ECMWF error from the combined error allowed an estimation of the global observation error. In addition to this error analysis we investigated the possible error resulting from the local time sampling of the CHAMP satellite. However, evidence was found that the discrete sampling of the CHAMP satellite in time, resulting in a bimodal distribution of the RO measurements in the local time, has only a small influence on the sampling error.

Climatologies were set up with a gridding strategy in two different modes: one mode comprises a fixed number of equal-area longitude bins at all latitudes, leading to bin overlapping at high latitudes, the other mode is defined with non-overlapping almost equal area bins with a latitude dependent number of longitude bins. Climatologies were arranged in a $10° \times 15°$ and $10° \times 60°$ binning as well as in zonal means. In addition to the dry temperature CHAMP climatologies, error fields were presented, which were derived with reference to ECMWF operational analysis fields. Coarser gridding leads to smaller climatological error.

For the zonal mean climatologies, the climatological errors amount to typically < 0.5 K globally, except for some distinct regions. Above 30 km, the climatological error at most latitudes exceeds 1 K, which may be attributed to both the CHAMP data and the ECMWF analysis fields. In the southern polar vortex for season JJA 2003 the climatological error varies by about ± 3 K, which is mainly due to insufficient representation of the polar vortex in the ECMWF analysis field. Near the tropical tropopause the climatological error throughout both seasons consistently amounts to around 1.5 K, which is probably due to weak representation of tropical tropopause variability in the ECMWF analysis fields. Further studies in these respects are on-going. For the purpose of characterizing and validating the pre-operational retrieval and processing system, the results of this type of climate diagnostics with reference to ECMWF data are very encouraging for proceeding as a next step to an operationalization of the system.

Acknowledgments

The authors gratefully acknowledge the GFZ Potsdam, Germany, for the provision of the CHAMP level 2 and level 3 correlative data, for technical support, especially provided by T. Schmidt, and for scientific discussion and advice provided by J. Wickert. We thank M. Fisher (ECMWF Reading) and A. Löscher (DMI Copenhagen) for providing error specifications for ECMWF analyses. J. Fritzer and J. Ramsauer provided helpful assistance regarding modification and use of the EGOPS software. We thank A. Simmons (ECMWF Reading), and S.S. Leroy (Harvard University) for valuable scientific discussions, and E. Manzini (INGV Bologna) and L. Kornblueh (MPI-M Hamburg) for their support and the provision of ECHAM5 data. Atmospheric analysis data for reference and validation were received from ECMWF.

M. Borsche and A. Gobiet received financial support for the work from the CHAMPCLIM project funded by the Austrian Ministry for Traffic, Innovation, and Technology and managed under Contract No. ASAP-WV-203/05 of the Austrian Aeronautics and Space Agency (FFG-ALR). Furthermore, A.K. Steiner, U. Foelsche, and A. Gobiet received financial support from the START research award of G. Kirchengast funded by the Austrian Ministry for Education, Science, and Culture and managed under Program No. Y103-N03 of the Austrian Science Fund (FWF).

List of References

Borsche, M., Gobiet, A., Steiner, A., Foelsche, U., Kirchengast, G., Schmidt, T., and Wickert, J. (2006). Pre-operational retrieval of radio occultation based climatologies within the CHAMPCLIM project. In U. Foelsche, G. Kirchengast, and A. Steiner, editors, *Proceedings to OPAC-2*. Springer.

Christy, J. and Spencer, R. (2003). Reliability of satellite data sets. *Science*, **301**, 1046–1047.

Foelsche, U. and Kirchengast, G. (2004). Sensitivity of GNSS radio occultation profiles to horizontal variability in the troposphere: A simulation study. In G. Kirchengast, U. Foelsche, and A. Steiner, editors, *Occultations for Probing Atmosphere and Climate*, pages 127–136. Springer.

Foelsche, U., Kirchengast, G., and Steiner, A. (2003). Global climate monitoring based on CHAMP/GPS radio occultation data. In C. Reigber, H. Luehr, and P. Schwintzer, editors, *First CHAMP mission results for gravity, magnetic and atmospheric studies*, pages 397–407, Berlin. Springer.

Foelsche, U., Gobiet, A., Steiner, A., Kirchengast, G., Borsche, M., Schmidt, ., and Wickert, J. (2006). Global Climatologies based on Radio Occultation Data: The CHAMPCLIM Project. In Foelsche, G. Kirchengast, and U. A. Steiner, editors, *Proceedings to OPAC-2*. Springer.

Gobiet, A. and Kirchengast, G. (2004a). Advancements of GNSS radio occultation retrieval in the upper stratosphere for optimal climate monitoring utility. In G. Kirchengast, U. Foelsche, and A. Steiner, editors, *Occultations for Probing Atmosphere and Climate*, pages 137–148. Springer.

Gobiet, A. and Kirchengast, G. (2004b). Advancements of GNSS radio occultation retrieval in the upper stratosphere for optimal climate monitoring utility. *J. Geophys. Res.*, **109**, doi: 10.1029/2004JD005117.

Gobiet, A., Steiner, A. K., Retscher, C., Foelsche, U., and Kirchengast, G. (2004). Radio Occultation Data and Algorithms Validation Based on CHAMP/GPS Data. Technical Report for ASA No. 1/2004, IGAM, University of Graz, Austria.

Gobiet, A., Foelsche, U., Steiner, A., Borsche, M., Kirchengast, G., and Wickert, J. (2005). Climatological validation of stratospheric temperatures in ECMWF operational analyses with CHAMP radio occultation data. *Geophys. Res. Lett.*, **32**, L12806, doi:10.1029/2005GL022617.

Healy, S., Jupp, A., and Marquardt, C. (2005). Forecast impact experiment with GPS radio occultation measurements. *Geophys. Res. Lett.*, **32**, L03804, doi:10.1029/2004GL020806.

Hedin, A. (1991). Extension of the MSIS thermosphere model into the middle and lower atmosphere. *J. Geophys. Res.*, **96**, 1159 – 1172.

Hocke, K., Igarashi, K., and Tsuda, T. (2003). High-resolution profiling of layered structures in the lower stratosphere by GPS occultation. *Geophys. Res. Lett.*, **30(8)**, 1426, doi: 10.1029/2002GL016566.

Hollingsworth, A. and Lönnberg, P. (1986). The statistical structure of short range forecast errors determined from radiosonde data. Part I: The wind field. *Tellus*, **38A**, 111–136.

Houghton, J. T., Ding, Y., Griggs, D., Noguer, M., van der Linden, P., Dai, X., Maskell, K., and Johnson, C., editors (2001). *Climate Change 2001: The Scientific Basis*. Cambridge University Press, Cambridge.

Kirchengast, G., Fritzer, J., and Ramsauer, J. (2002). End-to-end GNSS Occultation Performance Simulator Version 4 (EGOPS 4) Software User Manual (Overview and Reference Manual). Technical Report for ESA/ESTAC No. 3/2002, Inst. for Geophys., Astrophys., and Meteorol. (IGAM), Univ. of Graz, Austria.

Kuo, Y.-H., Sokolovskiy, S., Anthes, R., and Vandenberghe, F. (2000). Assimilation of GPS radio occultation data for numerical weather prediction. *Terr Atmos Oceanic Sci*, **11**, 157–186.

Kuo, Y.-H., Wee, T.-K., Sokolovskiy, S., Rocken, C., Schreiner, W., Hunt, D., and Anthes, A. (2004). Inversion and error estimation of GPS radio occultation data. *J Meteorol Soc Japan*, **82**, 507–531.

Kursinski, E., Hajj, G., Schofield, J., Linfield, R., and Hardy, K. (1997). Observing Earth's atmosphere with radio occultation measurements using the Global Positioning System. *J Geophys Res*, **102**, 23429–23465.

Löscher, A., Foelsche, U., and Kirchengast, G. (2005). CHAMPCLIM Midterm Report to ALR: Assimilation System Report. Technical Report for FFG-ALR No. 2/2005, IGAM, University of Graz, Austria.

Schmidt, T., Wickert, J., Beyerle, G., R.Koenig, Galas, R., and C.Reigber (2005). The CHAMP Atmospheric Processing System for Radio Occultation Measurements. In C. Reigber, H. Luehr, P. Schwintzer, and J. Wickert, editors, *Earth Observation with CHAMP: Results from Three Years in Orbit*, pages 597–602, Berlin. Springer.

Smith, E. and Weintraub, S. (1953). The constants in the equation for atmospheric refractive index at radio frequencies. In *Proc of the IRE 41*, pages 1035–1037.

Steiner, A. and Kirchengast, G. (2004). Ensemble-based analysis of errors in atmospheric profiles retrieved from GNSS radio occultation data. In G. Kirchengast, U. Foelsche, and A. Steiner, editors, *Occultations for Probing Atmosphere and Climate*, pages 149–160. Springer.

Steiner, A. and Kirchengast, G. (2005). Error analysis for GNSS radio occultation data based on ensembles of profiles from end-to-end simulations. *J. Geophys. Res.*, **110**. D15307, doi:10.1029/2004JD005251.

Steiner, A., Kirchengast, G., Foelsche, U., Kornblueh, L., Manzini, and Bengtsson, L. (2001). GNSS occultation sounding for climate monitoring. *Phys Chem Earth*, **26**, 113–124.

Steiner, A., Gobiet, A., Foelsche, U., and Kirchengast, G. (2004). CHAMPCLIM-Radio occultation data analysis advancement and climate change monitoring based on the CHAMP/GPS experiment. Technical Report for ASA No. 3/2004, IGAM, University of Graz, Austria.

Syndergaard, S. (1999). Retrieval analysis and methodologies in atmospheric limb sounding using the GNSS radio occultation technique. Technical Report for ASA No. 1/2004, Danish Meteorol. Inst., Copenhagen, Denmark.

Syndergaard, S., Flittner, D., Kursinski, R., Feng, D., Herman, B., and Ward, D. (2004). Simulating the influence of horizontal gradients on retrieved profiles from ATOMS occultation

measurements - a promising approach for data assimilation. in Occultations for Probing Atmosphere and Climate. In G. Kirchengast, U. Foelsche, and A. Steiner, editors, *Occultations for Probing Atmosphere and Climate*, pages 221–232. Springer.

Syndergaard, S., Kuo, Y.-H., and Lohmann, M. (2006). Observation operators for the assimilation of occultation data into atmospheric models: A review. In U. Foelsche, G. Kirchengast, and A. Steiner, editors, *Proceedings to OPAC-2*. Springer.

Vinnikov, K. and Grody, N. (2003). Global warming trend of mean tropospheric temperature observed by satellites. *Science*, **302**, 269–272.

Vorob'ev, V. and Krasnil'nikova, T. (1994). Estimation of the accuracy of the atmospheric refractive index recovery from Doppler shift measurements at frequencies used in the NAVSTAR system. *Phys Atmos Ocean*, **29**, 602 – 609.

Wickert, J., Beyerle, G., Schmidt, T., Michalak, G., Knig, R., and Reigber, C. (2005a). atmospheric profiling with CHAMP: Status of the operational data analysis, validation of the recent data products and future prospects. In C. Reigber, H. Lühr, P. Schwintzer, and J. Wickert, editors, *Earth Observations with CHAMP: Results from Three Years in Orbit*. Springer.

Wickert, J., Schmidt, T., Beyerle, G., Knig, R., Reigber, C., and Jakowski, N. (2005b). The radio occultation experiment aboard CHAMP: Operational data analysis and validation of vertical atmospheric profiles. *Special issue of J Met Soc Japan: Application of GPS Remote Sensing to Meteorology and Related Fields*, **1B**, 82.

WMO (1957). Definition of the tropopause. In *WMO Bull.,6*.

– end of document –